

Random time-shift approximation enables hierarchical Bayesian inference of mechanistic within-host viral dynamics models on large datasets

Dylan J. Morris^{1*}, Lauren Kennedy¹ and Andrew J. Black¹

¹ School of Computer and Mathematical Sciences, University of Adelaide, Adelaide, SA, Australia

* dylan.morris@adelaide.edu.au

Abstract

Mechanistic mathematical models of within-host viral dynamics are tools for understanding how a virus' biology and its interaction with the immune system shape the infectivity of a host. The biology of the process is encoded by the structure and parameters of the model that can be inferred statistically by fitting to viral load data. The main drawback of mechanistic models is that this inference is computationally expensive because the model must be repeatedly solved. This limits the size of the datasets that can be considered or the complexity of the models fitted. In this paper we develop a much cheaper inference method by implementing a novel approximation of the model dynamics that uses a combination of random and deterministic processes. This approximation also properly accounts for process noise early in the infection when cell and virion numbers are small, which is important for the viral dynamics but often overlooked. Our method runs on a consumer laptop and is fast enough to facilitate a full hierarchical Bayesian treatment of the problem with sharing of information to allow for individual level parameter differences. We apply our method to simulated data and a reanalysis of COVID-19 monitoring data in an National Basketball Association cohort of 163 individuals.

Author summary

Understanding how viruses reproduce within an infected host is crucial for predicting disease progression and evaluating treatments. One way to study this is by using mathematical models that describe how viruses reproduce in the body, such as in the respiratory tract. These models help understand key biological processes, but they require significant computing power, making it difficult to analyse data from large groups of individuals. In this study we developed a new, faster, method for analysing viral load data. Our approach combines randomness, to account for chance events early in infection, with a more predictable model once the infection is well established. This allows us to speed up calculations while capturing key biological processes and maintaining a high degree of accuracy. Our method is efficient enough to run on a laptop, making it possible to study large datasets using a full statistical approach that accounts for individual differences. We tested our method on simulated data and applied it to real-world data from 163 individuals in a COVID-19 monitoring study. Our results show that the model can accurately estimate key parameters and track viral load dynamics over time.

1 Introduction

Within-host viral dynamics (WHVD) models describe the progression of viral levels within an individual post-infection [1–3]. Depending on their complexity, these models can capture key biological processes such as viral replication, immune response, and clearance, or focus on summarising features like peak timing and growth/decline rates [1–4]. In a typical acute infection, the amount of virus in an individual—referred to as the viral load (VL)—grows exponentially before peaking (due to the immune response and / or the carrying capacity of the respiratory tract) before declining [5]. Modelling this progression of virus inside a host can provide insight into important features like when an individual’s infectiousness (VL) peaks, differences between variants of a disease, and the vaccination status of individuals [6], all of which are drivers of between-host (or transmission) dynamics [7–9] and are key in informing health policies [10].

Mathematical models of WHVDs are broadly either phenomenological or mechanistic [4, 5, 11]. Phenomenological models are typically regression models that are able to capture key observed macroscopic (measurable) quantities like growth and decline rates as well as the timing of the peak of infection [4, 11]. Such models can provide a good fit to data and predictions of the viral load trajectory but do not yield any understanding of the underlying biology of the system. Mechanistic modelling overcomes this by constructing models that explicitly track the populations of cells and virus in a region of the body [5, 12–15]. Typically such a model is specified in terms of the biological interactions of the lower level entities from which solutions for the macroscopic viral load can be derived or simulated. The major drawback of such models is that they are much more expensive to fit to data because they do not have simple parametric solutions. One of the main contributions of our work here is to develop a radically faster inference approach, such that fitting complicated mechanistic models is now possible on basic consumer hardware.

Our second main contribution is that we can fit a fully stochastic model, instead of a only a deterministic one. To put this in context, mechanistic models are themselves broadly either stochastic or deterministic. Deterministic models are much cheaper to solve, but stochastic models capture random variation from when the populations are initially small (i.e. early in the infection) that can still have an impact on the time for the viral load to peak [16, 17]—ignoring this effect potentially biases inferences. The additional complexity of stochastic models has lead—with one exception [18]—to most inference approaches ignoring early time noise and only fitting simple deterministic models for the mean populations [5, 8, 11]. In this work we leverage the large scales over which the VL changes (from 10^0 to 10^8 virons per μl of plasma) to derive a novel approximation for the solutions of a fully stochastic WHVD model. This facilitates our first contribution by allowing the derivation of a fast and accurate approximation to the likelihood for VL time-series data. It also properly takes account of the early stochasticity in the process that is required for performing unbiased inference.

Our method is so fast that it allows for fitting a full hierarchical Bayesian model to datasets of hundreds of individuals such as the COVID19 testing dataset collected from National Basketball Association (NBA) players during the 2020-2021 seasons [4, 6]. This dataset is one of the most complete and detailed datasets publicly available that features longitudinal measurements of individuals’ VL’s through time, using common data formats found in the literature [2, 5, 11, 19, 20]. In contrast to others [4–6, 18], we fit a full stochastic model to all 163 measured individuals and the inference algorithm is run on a consumer laptop in approximately one hour. The method can produce accurate posterior predictive VL trajectories and parameter estimates of the key within-host parameters (e.g. the within-host basic reproduction number, R_0) that are consistent with previous studies of respiratory illnesses [2, 5, 11, 19]. The hierarchical

structure of the model allows us to share information from individuals with sufficient data to those whose data is limited, or noisy, during the growth and/or the decline phases of the infection. Our method can be easily extended to other datasets and other within-host models (i.e. models that include immune responses [8, 21]) and other viral infections and so provides a general tool for fitting to WHVD data.

The key idea upon which our method builds is that the macroscopic dynamics of a fully stochastic WHVD model can be accurately approximated using a deterministic model with a random time-shift applied to the initial conditions [16, 17]. Fig. 1 illustrates this random time-shift idea. In Fig. 1A, the grey lines show realisations of a stochastic model (defined fully later) and the black line shows the deterministic approximation to the stochastic model. At early times the process is strongly affected by stochasticity due to the small numbers of cells and virions, but this occurs below a detection threshold (indicated by the horizontal red line) where data is not available. Once the virion numbers grow large enough, growth becomes exponential, and appears deterministic. The early time stochasticity is reflected on the macroscale (the scale on which measurements can be made, i.e. above the detection threshold) in the time for the virus to peak. We see that the deterministic model (black line) accurately captures the growth and decline rates as well as the peak height, but not the randomness in the time to peak. But, by time shifting the initial conditions of the deterministic trajectory—keeping the initial numbers fixed—the model can capture the randomness in the time to peak. The orange curve in Fig. 1B shows the density of this random variable; our previous work details how this can be accurately approximated by a closed form function that can be calculated for a given model [17].

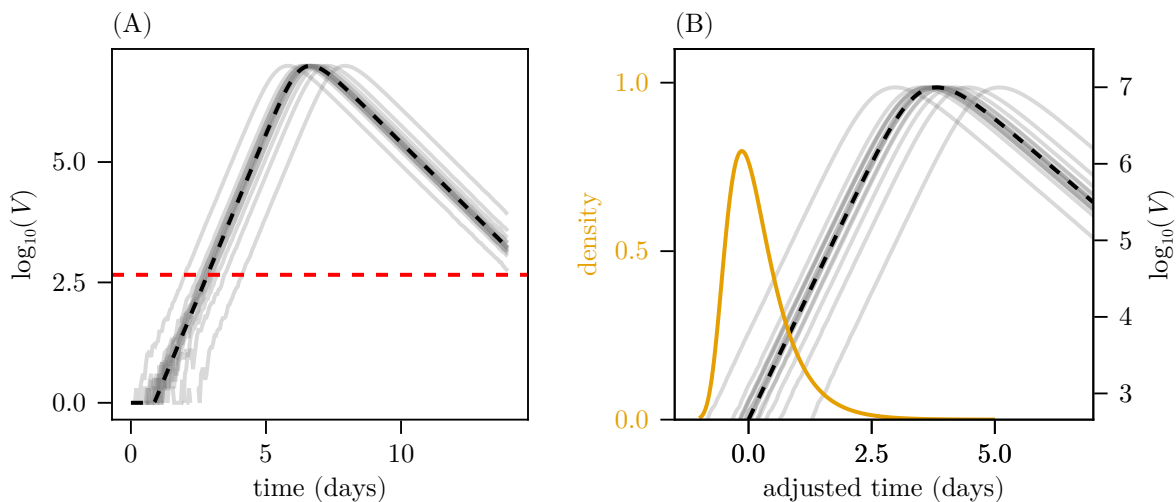


Fig 1. Illustration of the time-shift concept. (A) Example simulations from the fully stochastic model (grey lines) and the deterministic approximation (black). The detection limit for observations is indicated by the red dashed line. (B) The same simulations as shown in panel (A) but starting the plot from when the simulations cross the detection limit. Translating the deterministic trajectory through time approximates the stochastic solutions on the macroscale. The orange curve shows the probability density of this shift, defined by aligning threshold-crossing times and is equivalent to a shift in the initial conditions of the deterministic model. The models and parameters are described in Sections 2.1 and 2.2, with $\theta = (8, 4, 1.7, 3, 10, 0)$ used in these simulations.

Within-host models are an ideal system for an application of this approximation method because the approximation is most accurate where we have data, i.e. when the populations have grown significantly. During the initial stages of the infection when virus and infected cell numbers are small, the approximation is less accurate, but in this region data is effectively unavailable anyway because there is a detection threshold for measurements (i.e. the data is censored) [2, 5, 11, 19]. The important effect of stochasticity in this early time regime is to shift the time-to-peak, and this is captured accurately by the approximation.

Another way of looking at this approximation is that it allows for fast forward simulation of the model without the need for costly stochastic simulation, for example using the Gillespie algorithm [22, 23]. So for a given set of parameters, all that is required is a *single* solution of the deterministic model and samples from the corresponding time-shift distribution. In doing the inverse, i.e. inference of model parameters from data, adopting the time-shift approximation is also enlightening. In many existing studies of this problem the initial viral load is treated as being unobserved and hence a parameter to be inferred [11] or fixed at some value [5]. The time-shift idea facilitates a shift in perspective from inferring the initial viral load at a fixed time, to instead inferring a fixed viral load at a random time. This turns out to be a key insight as it allows the derivation of a number of further accurate approximations for the likelihood function that provide large computational speed ups, allowing inference on large datasets using a relatively complicated model.

We begin in Section 2 by outlining our particular stochastic viral kinetics model and show mathematically how the dynamics can be approximated using the time-shift ideas. We then provide details of approximations that can be made as a result of how the time-shift is incorporated into the likelihood in order to improve the efficiency of our inference method. This provides the foundations for a Metropolis-Hastings within Gibbs sampler for sampling from the posterior distribution. In Section 3 we apply it to two datasets. Firstly, a synthetic data set that is used to validate the method and quantify its inference capabilities in a context where the true values of the parameters are known. We find that our approach is able to disentangle the measurement noise from the process noise and results in parameter estimates that are more consistent with the simulated parameters. Secondly, we fit the model to the NBA COVID-19 dataset [4, 6] where we find that our posterior predictive fits indicate that the method is able to produce a realistic fit to the data and obtain R_0 estimates that are consistent with previous studies. Additionally we show that the method is able to share information across individuals, to those with few observations and missing data, to estimate their viral dynamics. All the data and code are available in the following GitHub repository: https://github.com/djmorris7/random_time_shift-within_host_inference.

2 Materials and methods

2.1 The viral kinetics model

In this work we consider one of the simplest viral kinetics model referred to as the Target-Cell-Limited (\mathcal{TCL}) model with an eclipse-phase [2, 24, 25]. This model captures the basic cell infection cycle and viral production cycles observed during an infection while accounting for an appropriate delay (the eclipse phase) between a cell becoming infected and producing virus. We choose this simpler model and not something more complex (see [14] for an example) as some of the parameters are already unidentifiable from VL data [25, 26] and so adding more complexity without additional data sources only exacerbates this. The method itself can easily be applied to more complex models if required. The \mathcal{TCL} model is commonly specified as a set of (deterministic) ordinary

differential equations [2, 24, 27] for the total population counts, but here we will instead start with a stochastic version that captures the individual nature of the populations from which we will derive the random time-shift approximation consisting of a deterministic ODE and the time-shift distribution itself.

The \mathcal{TCC} model tracks the numbers of susceptible target cells, $S(t)$, cells in the eclipse phase, $E(t)$, infected cells, $I(t)$, and free virus, $V(t)$, in an effective volume K , corresponding to the volume over which the within-host infection process occurs. The dynamics of these populations are modelled as a continuous-time Markov chain (CTMC) [28, 29] $\{\mathbf{X}(t), t \geq t_0\}$ where t_0 is the time at which the infection is initiated, and is unknown, and the state of the system at time $t \geq t_0$ is specified by the vector $\mathbf{X}(t) = (S(t), E(t), I(t), V(t))$. Adopting this formulation means that populations are non-negative integers. Target cells are uninfected cells that become infected when virus binds to them, a process that follows mass action kinetics [2, 30]. The instantaneous rate at which target cells become infected is given by $\alpha S(t)V(t)/K$, where α represents the per-virus infection rate of target cells. In most formulations of this model [1, 2, 5, 27], the parameter $\beta = \alpha/K$ is the parameter of interest. For consistency, we also take β as the parameter of interest in our model. Following infection, cells enter an eclipse phase, which follows an exponential distribution with mean $1/\sigma$ days, during which infected cells are not yet actively producing virus. Infectious cells are then removed (either by immune clearance or cell death) after an exponentially distributed time with mean $1/\delta$ days. While infected, cells produce new virions at rate ρ copies per day, which are cleared at rate c per day, due to immune response or other clearance mechanisms. The state transitions and rates of the model are summarised in Table 1.

Event	$\Delta \mathbf{X}$	Rate
Infection	$(-1, +1, 0, 0)$	$\beta S(t)V(t)$
Cell becomes infectious	$(0, -1, +1, 0)$	$kE(t)$
Infectious cell recovery	$(0, 0, -1, 0)$	$\delta I(t)$
Production of virus	$(0, 0, 0, +1)$	$\rho V(t)$
Clearance of virus	$(0, 0, 0, -1)$	$cV(t)$

Table 1. Rates for the CTMC viral dynamics model. Each row gives an event type, the associated change in state $\mathbf{X}(t)$, and the rate at which the event occurs in the \mathcal{TCC} model.

There is a choice to be made regarding the initial condition, $\mathbf{X}(0)$. The infection is triggered by the entry of virus into the system, so ideally, the initial viral load, $V(0)$, would be set. However, this introduces complexity regarding the amount of virus required to cause an infection [12, 31]. Jones et al. [31] show that the dynamics of the model are not significantly altered by taking the initial condition as a single infected cell, as any initial viral particles must initiate an infection by infecting one or more cells (at a rapid rate) before being cleared. Throughout this work we assume that $S(0) = 8 \times 10^7$ based on Zitzmann et al. [5]. Hence, throughout this work, we consider viral infections triggered by a single infected (but not actively infectious) cell, i.e., the initial condition is $\mathbf{X}(0) = (S(0) - 1, 1, 0, 0)$. The methods presented here can be extended to handle more complex initial conditions, and extensions of this are discussed in Section 4.

A pivotal quantity in such models is the basic reproduction number R_0 , which is defined as the average number of secondary infected cells that are produced by an initially infected cell when the target cell population is fully susceptible [32]. The importance of this quantity is that it is a measure of the virus' ability to invade the population of susceptible cells and result in an acute infection [33]. If $R_0 \leq 1$ then the virus will die out before infecting a large number of cells. If $R_0 > 1$ then there is a chance that the virus will invade the cell population and result in an acute infection.

The basic reproduction number for this model can be computed through the next generation matrix method [34] and is given by [5],

$$R_0 = \frac{\beta S(0)\rho}{\delta c}. \quad (1)$$

2.2 Random time-shift approximation

Here, we show that the macroscopic dynamics of the stochastic model described in Section 2.1 can be approximated by a deterministic ODE model, which corresponds to standard formulations with an added random time shift to the initial conditions. The deterministic approximation follows from a mean-field approximation of the CTMC model in the limit $K \rightarrow \infty$ (i.e., for large volume). In the context of respiratory infections, K corresponds to the total volume over which the within-host infection process occurs and can therefore be considered “large” in the sense that the number of interacting particles (e.g., cells and virions) is sufficiently high. Throughout this work, however, the exact value of K is unimportant, as it can be absorbed into the model parameters. Let $s(t) = S(t)/K$, $e(t) = E(t)/K$, $i(t) = I(t)/K$ and $v(t) = V(t)/K$ denote the densities of the cell and virus populations of each type, then in the limit as $K \rightarrow \infty$ these evolve via a set of coupled ODEs (see Section 1 of [S1 text](#) for derivation) [35])

$$\begin{aligned} \frac{ds(t)}{dt} &= -\alpha s(t)v(t), \\ \frac{de(t)}{dt} &= \alpha s v(t) - k e(t), \\ \frac{di(t)}{dt} &= k e(t) - \delta i(t), \\ \frac{dv(t)}{dt} &= \rho i(t) - c v(t). \end{aligned} \quad (2)$$

We can multiply Eqs. (2) through by the volume K as it is large and fixed to obtain the system of ODEs that govern the approximation for the mean dynamics [2, 5]. We use the notation $S_d(t) = Ks(t)$, $E_d(t) = Ke(t)$, etc. with the subscript d identifying these variables as solutions of the deterministic system. Once more, for consistency between the stochastic and deterministic formulations, we make the substitution $\beta = \alpha/K$,

$$\begin{aligned} \frac{dS_d(t)}{dt} &= -\beta S_d(t)V_d(t), \\ \frac{dE_d(t)}{dt} &= \beta S_d(t)V_d(t) - kE_d(t), \\ \frac{dI_d(t)}{dt} &= kE_d(t) - \delta I_d(t), \\ \frac{dV_d(t)}{dt} &= \rho I_d(t) - cV_d(t). \end{aligned} \quad (3)$$

These equations match the ODEs that are usually just written down when working in a purely deterministic modelling paradigm [3, 5]. It is difficult to work with the transmission parameter β as it is strongly dependent on the experimental setup in the study of interest (i.e. what method is used to collect VL samples) and negatively correlated with ρ [5] so in this work we reparameterise the model in terms of R_0 (and back transform to obtain β when needed) and hence the parameters are collected in the vector $\boldsymbol{\theta} = (R_0, k, \delta, \rho, c, t_0)$.

Denote the solution of Eqs. (3), $\mathbf{X}_d(t) = (S_d(t), E_d(t), I_d(t), V_d(t))$, then this provides an approximation to the mean dynamics of the full stochastic CTMC

$\{\mathbf{X}(t), t \geq t_0\}$, but does not capture the effect of the noise during the early-time phase when the numbers of infected cells and virions is low (see Fig. 1 and discussion in Section 1). The predominant effect of the stochasticity is to shift the time at which the peak VL occurs and subsequently the time at which the infection is cleared [16, 17, 36]. The work of Barbour et al. [16] formalises the connection between the shifted mean field kinetics and samples of the full stochastic process. They show that $\{\mathbf{X}(t), t \geq t_0\}$ is well approximated on the macroscale, i.e. the growth and decline rates and peak time and height, by another stochastic process $\{\mathbf{X}_d(t + \tau), t \geq t_0\}$ where $\tau := \tau(\boldsymbol{\theta}) \in \{-\infty\} \cup \mathbb{R}$ is a scalar random variable referred to as the *random time-shift* [16, 17].

The practical importance of this result is that sample paths of $\{\mathbf{X}(t), t \geq t_0\}$ resemble those of the deterministic model, $\mathbf{X}_d(t)$, except for a translation in time by the time-shift τ . The case $\tau = -\infty$ corresponds to when the number of virions and infected cells drops to zero, i.e. extinction of the virus within the host. Our interest lies in the modelled VL once $V(t)$ has grown to be measurable, i.e. outside of the early-time small population regime. Approximating the stochastic process $\{\mathbf{X}(t), t \geq t_0\}$ in this way means we can efficiently generate sample paths $V(t)$ by solving for the mean field kinetics and obtaining the distribution of the time-shift. The process $\{\mathbf{X}_d(t + \tau), t \geq t_0\}$ does not capture the noisy early dynamics (i.e. the actual stochastic fluctuations in the populations when these counts are small) but this is of little consequence as small VL's fall below a detection threshold and are therefore not measurable [4, 5, 11].

The distribution of the random variable τ is derived by analysing a branching process approximation to the early time dynamics and can be expressed as the mixture [17]

$$F(\tau | \boldsymbol{\theta}) = q^*(\boldsymbol{\theta}) + (1 - q^*(\boldsymbol{\theta})) \int_{-\infty}^{\tau} f(t | \boldsymbol{\theta}) dt, \quad \tau \in \{-\infty\} \cup \mathbb{R}, \quad (4)$$

where $q^*(\boldsymbol{\theta})$ is the probability of ultimate extinction and the term inside the integrand, $f(\tau | \boldsymbol{\theta})$, is the density function for τ conditional on non-extinction. As a result of the simplicity of the \mathcal{TCL} model, $q^*(\boldsymbol{\theta})$, can be solved for analytically by solving a set of non-linear equations (see Section 2 of S1 text). In previous work [17] we showed that the density function for τ , conditional on non-extinction, can be accurately approximated by a member of a family of functions with the form

$$f(\tau | \boldsymbol{\theta}) = \frac{p\lambda\mu_W^d}{a^d\Gamma\left(\frac{d}{p}\right)} \exp\left(-\left(\frac{\mu_W e^{\lambda\tau}}{a}\right)^p + \lambda\tau d\right) \quad (5)$$

with (a, d, p) determining the particular member of the family. The quantity λ —the early growth rate of the model—and the time-shift parameters $\boldsymbol{\zeta} = (a, p, d)$ are numerically calculated from the branching process approximation to the CTMC (see [17] for concrete examples). The red curve shown in Fig. 1 is this density evaluated for the given parameters. Recall that as τ is a function of $\boldsymbol{\theta}$, the parameters $\boldsymbol{\zeta}$ are also a function of $\boldsymbol{\theta}$ but that this has been suppressed in the notation for clarity. One final and important point is that the time-shift is independent of the infection time t_0 .

2.3 Viral load measurement model

The data we assume available for each individual is a time-series of the \log_{10} viral load (log-VL) measurements, denoted $\mathbf{y} := (y_1, \dots, y_J)$, where $y_j := y_{t_j}$ is the log-VL at time t_j . In practice the t_j could be determined in a variety of ways depending on the data-collection process. For a longitudinal study like that run on the NBA cohort [4], daily observations are taken over a long period of time and only the start point of the time-series is effectively random. In a household study, for example, the first time for each individual in a given household is intrinsically linked to both the household being

first tested and could come after individuals are infectious, meaning that the first times are random for each index case [37]. Additionally, the timings of the test between individuals are likely to be non-equidistant and also prone to variability as well. The data is right-censored at a threshold η (i.e. $y_j = \eta$ means that $y_j \leq \eta$) which describes the limit of detection of the assay used to measure the viral load [4, 11, 12].

We assume that the data for a single individual are noisy measurements of some underlying VL trajectory. Once more we note that the time-shift, τ , is a random variable that is a function of the VL model parameters, θ and that $V_d(t, \theta)$ now has explicit dependence on the VL model parameters θ . Inclusion of the time-shift means that the modelled trajectory is effectively translated in time and so the modelled trajectory is effectively delayed or advanced depending on the sign of the time-shift. In the case where there is a slow start to infection (i.e. a negative time-shift) the modelled trajectory is translated to the right and so is effectively delayed. To handle inconsistencies with the modelled trajectory from applying the time-shift we simply set the VL over this time to the initial condition. For the case where the time-shift is positive, the opposite is true and the modelled trajectory is effectively translated to the left. In this case we can use the modelled trajectory without changes. The only other consideration is that the time t we evaluate the modelled trajectory at must be after the infection time, i.e. $t \geq t_0$. This can be summarised by defining

$$z(t, \tau, \theta) = \begin{cases} \log_{10} V_d(t + \tau, \theta), & \text{if } t + \tau > t_0 \\ -\infty, & \text{if } t + \tau \leq t_0 \text{ or } t \leq t_0. \end{cases} \quad (6)$$

Let $\mathbf{z}(\tau) := (z_1(\tau), \dots, z_J(\tau))$ denote the modelled viral load at the observation times (t_1, \dots, t_J) for a particular time-shift τ , that is $z_j(\tau) := z_{t_j}(\tau) := z(t_j, \tau, \theta)$. Throughout this work we will use the convention that normal distributions are parameterised in terms of mean and standard deviation, i.e. $\mathcal{N}(\mu, \sigma)$, as this parallels the formulation in the code. We assume that the observations are noisy measurements of the modelled trajectory, $y_j = z_j(\tau) + \epsilon_j$ and $\epsilon_j \sim \mathcal{N}(0, \kappa)$ for $j = 1, \dots, J$ and some standard deviation κ , which is assumed to be unknown.

To provide further clarity on the idea of the time-shift and how this connects to the complete data generation process we now illustrate the idea in the context of a forward simulation framework. Algorithm 1 details the key steps to simulate an approximate stochastic realisation of the WHVD model given model parameters θ . This process assumes some discrete times that the stochastic trajectory is sampled at and a particular value of the scale parameter for the observation noise, κ .

Algorithm 1 Forward simulations using time-shifts

Inputs:

- The WHVD model parameters θ .
- Observation times $\mathbf{t} = (t_1, \dots, t_J)$.
- Scale parameter on the observation noise, κ .

- 1: Solve Eqs. (3) to get the deterministic trajectory $V(t)$ through time.
 - 2: Compute the time-shift parameters $\zeta = (a, d, p)$ using methods in Morris et. al [17].
 - 3: Sample $\tau \sim f(\tau | \theta)$ (given by Eq. (5)).
 - 4: Shift $V(t)$ via Eq. (6) to get the approximate stochastic trajectory $z(t, \tau, \theta)$.
 - 5: **Return** $z(t, \tau, \theta)$.
-

2.4 Mixed effects model

In this section we provide the general form (deferring details of the calculation of the likelihood and specific priors to Sections 2.6 and 2.5, respectively) of our mixed effects

model. This includes detailing the data and writing down the posterior distribution.

We assume a simple experimental setup of a sample of N individuals where θ_i denotes the VL model parameters for individual i and $\mathbf{y}_i = (y_{i,1}, \dots, y_{i,J_i})$ denotes the time-series of their measured VL, which consists of J_i observations. Define $\Theta = \{\theta_1, \dots, \theta_N\}$ and $\mathcal{D} = \{\mathbf{y}_1, \dots, \mathbf{y}_N\}$ as the collections of parameters and data, respectively. We assume that the subject specific parameters, θ_i 's, are distributed according to some population distribution on what we refer to as shared parameters ϕ (the exact relationships are defined in Section 2.6). Relationships between the components in the model are depicted in the plate diagram shown in Fig. 2 where the direction of the arrows dictates dependencies between parameters, hyper-parameters and data.

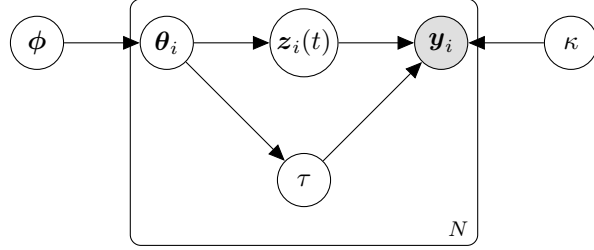


Fig 2. Plate diagram of the relationship between components in the model. The plate indicates individual level variables that are indexed by the number of individuals, N . The parameters outside the plate, ϕ and κ , are shared across all individuals.

The joint posterior distribution of the model parameters and the shared parameters is given by

$$f(\Theta, \phi, \kappa | \mathcal{D}) \propto f(\mathcal{D} | \Theta, \kappa) f(\Theta | \phi) f(\phi) f(\kappa), \quad (7)$$

where $f(\mathcal{D} | \Theta, \kappa)$ is the joint parameter-likelihood, and $f(\Theta | \phi)$, $f(\phi)$, and $f(\kappa)$ are prior distributions that are detailed in Section 2.6. Since the individuals are conditionally independent given their unique parameters, θ_i , we can factorise the joint-likelihood as

$$f(\mathcal{D} | \Theta, \kappa) = \prod_{i=1}^N f(\mathbf{y}_i | \theta_i, \kappa), \quad (8)$$

where $f(\mathbf{y}_i | \theta_i, \kappa)$ is the *marginal likelihood* function for individual i , as it is obtained by marginalising over the random time-shifts (see Section 2.5.1 for details). Conditional on the hyper-parameters, the prior $f(\Theta | \phi)$ can be factorised similarly, which results in a simpler form of the posterior

$$f(\Theta, \phi, \kappa | \mathcal{D}) \propto \left[\prod_{i=1}^N f(\mathbf{y}_i | \theta_i, \kappa) f(\theta_i | \phi) \right] f(\phi) f(\kappa). \quad (9)$$

The difficult part of evaluating Eq. (9) is in the calculation of the marginal likelihood terms, due to the need to marginalise over the distribution of trajectories as seen in Fig. 2.

2.5 Likelihood approximations

In this section, we outline the construction of the *marginal likelihood* for an individual, breaking it down into its components: the time-shift and the *path likelihood*—the likelihood function given a viral load (VL) sample path. This approach mirrors the

general method used in the literature for constructing the likelihood in purely deterministic models [5, 11, 38].

2.5.1 Marginal likelihood

The *marginal likelihood* (likelihood for individual i 's data, \mathbf{y}_i , given the parameters, $\boldsymbol{\theta}_i$) is given by $f(\mathbf{y}_i | \boldsymbol{\theta}_i, \kappa)$. Since the observation process depends on an unobserved random time-shift τ , we marginalise over τ

$$f(\mathbf{y}_i | \boldsymbol{\theta}_i, \kappa) = \int f(\mathbf{y}_i | \tau, \boldsymbol{\theta}_i, \kappa) dF(\tau | \boldsymbol{\theta}_i). \quad (10)$$

The likelihood given τ depends on the system's trajectory $\mathbf{z}_i(\tau)$, which is deterministic for a given τ and $\boldsymbol{\theta}$, so we can rewrite the conditional likelihood as

$$f(\mathbf{y}_i | \tau, \boldsymbol{\theta}_i, \kappa) = f(\mathbf{y}_i | \mathbf{z}_i(\tau), \boldsymbol{\theta}_i, \kappa). \quad (11)$$

The distribution of the random time-shift $F(\tau | \boldsymbol{\theta}_i)$ has a single point mass at $\tau = -\infty$, of size $q^*(\boldsymbol{\theta}_i)$, corresponding to extinction, where the likelihood of observing any data is zero. Excluding this case, the remaining portion of $F(\tau | \boldsymbol{\theta}_i)$ is absolutely continuous with density $f(\tau | \boldsymbol{\theta}_i)$, allowing us to write

$$f(\mathbf{y}_i | \boldsymbol{\theta}_i, \kappa) = (1 - q^*(\boldsymbol{\theta}_i)) \int f(\mathbf{y}_i | \mathbf{z}_i(\tau), \boldsymbol{\theta}_i, \kappa) f(\tau | \boldsymbol{\theta}_i) d\tau. \quad (12)$$

Observations $y_{i,j}$ correspond to viral load (VL) measurements at times t_j , which are assumed to be independent given the model trajectory. The deterministic trajectory $z_{i,j}(\tau) := z(t_j, \tau, \boldsymbol{\theta}_i)$ represents the modelled VL at time t_j for individual i . Given $z_{i,j}(\tau)$, the conditional likelihood of the observed data \mathbf{y}_i is

$$f(\mathbf{y}_i | \mathbf{z}_i(\tau), \boldsymbol{\theta}_i, \kappa) = \prod_{j=1}^{J_i} f(y_{i,j} | z_{i,j}(\tau), \boldsymbol{\theta}_i, \kappa), \quad (13)$$

where the terms inside the product are given by

$$f(y_{i,j} | z_{i,j}(\tau), \boldsymbol{\theta}_i, \kappa) = \begin{cases} \mathcal{N}_{\text{PDF}}(y_{i,j} | z_{i,j}(\tau), \boldsymbol{\theta}_i, \kappa), & \text{for } y_{i,j} > \eta, \\ \mathcal{N}_{\text{CDF}}(\eta | z_{i,j}(\tau), \boldsymbol{\theta}_i, \kappa), & \text{for } y_{i,j} \leq \eta \end{cases}$$

where $\mathcal{N}_{\text{PDF}}(y_{i,j} | z_{i,j}(\tau), \boldsymbol{\theta}, \kappa)$ and $\mathcal{N}_{\text{CDF}}(\eta | z_{i,j}(\tau), \boldsymbol{\theta}, \kappa)$ are the probability density function, and cumulative distribution function, respectively, of a $\mathcal{N}(z_{i,j}(\tau), \kappa)$ random variable. The CDF terms account for observations below the detection threshold [11]. To distinguish this from other likelihood formulations, we refer to Eq. (13) as the *path-likelihood* for a single individual. The marginal likelihood, Eq. (12), can be evaluated by substituting in the path-likelihood, Eq. (13), but this is inefficient due to the numerical integration of an interpolated ODE solution. In Section 2.5.2 we develop a faster approximation which replaces this calculation.

We note here that if the VL model is replaced with the deterministic model without the time-shift, then this is equivalent to the time-shift density collapsing to a point mass at $\tau = 0$ and the removal of the extinction probability factor. Hence, the likelihood is simply $f(\mathbf{y}_i | \mathbf{z}_i(0), \boldsymbol{\theta}_i, \kappa)$ as often seen in VL kinetics modelling [5, 8, 11, 38].

2.5.2 Laplace approximation of the path likelihood

The marginal likelihoods (Eq. (12)) do not admit a simple closed form expression and so we resort to numerical integration. We use an adaptive Gauss–Kronrod quadrature for

numerical integration [39] as it is highly efficient and demonstrated strong performance in our testing. The challenge with evaluating the marginal likelihood directly is that it relies on repeated evaluation of the modelled viral-load. Repeating this calculation is necessary as we are integrating over τ which appears inside the ODE solution (i.e. $\mathbf{z}_i(\tau)$). To evaluate this, the ODE solution is interpolated and calling this inside a numerical integrator is computationally expensive.

To address this, we consider a Laplace approximation of the interior of the integral of the marginal likelihood [40, Chapter 27]. We evaluated two approaches: (1) constructing a Laplace approximation for the path-likelihood alone and then numerically integrating, or (2) constructing a Laplace approximation for the product of the path-likelihood and the time-shift distribution, and deriving a closed-form expression. The approximation of the path-likelihood alone was initially considered the more appropriate approach, as the path-likelihood is the product of normal PDFs (and few CDF values), and therefore, it is approximately a scaled Normal distribution (note that the scaling means this is a function, not a density). In contrast, the time-shift distribution is skewed (see Fig. 1). However, in our testing, we found that these two approaches produced comparable results, with the Laplace approximation of the product of the path-likelihood and time-shift distribution reducing the evaluation time of the likelihood by approximately 30%.

We begin the construction of the Laplace approximation by noting that the data, \mathbf{y}_i , VL model parameters, $\boldsymbol{\theta}_i$, and κ are assumed to be known and fixed. Define the functions

$$g(\tau) = f(\mathbf{y}_i | \mathbf{z}_i(\tau), \boldsymbol{\theta}_i, \kappa) f(\tau | \boldsymbol{\theta}_i), \quad h(\tau) = \log g(\tau).$$

Suppose there is a global maximum

$$\tau_0 = \arg \max_{\tau} g(\tau) = \arg \max_{\tau} h(\tau),$$

and define

$$H(\tau) = \sqrt{-\frac{1}{h''(\tau)}},$$

noting that the function is assumed to be concave (implicit in applying the Laplace approximation), which implies $h''(\tau) < 0$ around τ_0 , and hence $H(\tau) > 0$. Taylor expanding $h(\tau)$ about τ_0 and noting that $h'(\tau_0) = 0$ (since τ_0 is the maximum), we get

$$h(\tau) \approx h(\tau_0) + \frac{1}{2} h''(\tau_0) (\tau - \tau_0)^2 = h(\tau_0) - \frac{1}{2H(\tau_0)^2} (\tau - \tau_0)^2.$$

Then, we have

$$g(\tau) = \exp(h(\tau)) \approx g(\tau_0) \exp\left(-\frac{(\tau - \tau_0)^2}{2H(\tau_0)^2}\right).$$

Since $H(\tau_0) > 0$, this is the kernel of a $\mathcal{N}(\tau_0, H(\tau_0))$ random variable scaled by $g(\tau_0) = f(\mathbf{y}_i | \mathbf{z}_i(\tau_0), \boldsymbol{\theta}_i, \kappa)$. Substituting into Eq. (12), the Laplace approximation is

$$f(\mathbf{y}_i | \boldsymbol{\theta}_i, \kappa) \approx (1 - q^*(\boldsymbol{\theta}_i)) f(\mathbf{y}_i | \mathbf{z}_i(\tau_0), \boldsymbol{\theta}_i, \kappa) f(\tau_0 | \boldsymbol{\theta}_i) \int \exp\left(-\frac{(\tau - \tau_0)^2}{2H(\tau_0)^2}\right) d\tau.$$

Since the interior of the integrand is a Normal kernel, a closed-form approximation is given by

$$f(\mathbf{y}_i | \boldsymbol{\theta}_i, \kappa) \approx \sqrt{2\pi} (1 - q^*(\boldsymbol{\theta}_i)) f(\mathbf{y}_i | \mathbf{z}_i(\tau_0), \boldsymbol{\theta}_i, \kappa) f(\tau_0 | \boldsymbol{\theta}_i) H(\tau_0). \quad (14)$$

The mean of the Gaussian, τ_0 , can be estimated using numerical optimisation. The scale term $H(\tau_0)$ has a more complicated form but can be computed through either

numerical differentiation or automatic differentiation. In this work, all our code is written in the Julia programming language [41], and the package ForwardDiff.jl [42] enables efficient computation of exact derivatives through forward mode automatic differentiation for such codes.

In Section 4 of [S1 text](#), we plot profile likelihoods—i.e., the likelihood with all parameters fixed except for one, which is allowed to vary—for a simulated VL trajectory to show the accuracy of the approximation in Eq. (14) versus the exact calculation in Eq. (12). The profile likelihoods had a maximum (absolute) error of $< 10^{-7}$ at the tested points, which indicates strong agreement between our Laplace approximation and the exact likelihood.

2.6 Priors

In this section, we detail our choices of priors and fixed parameters. To ensure broad applicability, we center our priors at values consistent with studies on other viral infections (e.g., influenza) and COVID-19. To account for uncertainty in these estimates, we use weakly informative priors with higher variance. Prior predictive checks confirm that the effective priors on individual parameters remain weakly informative. It is important to note that our primary focus is methodological—demonstrating how to incorporate stochasticity into WHVD models—rather than obtaining precise parameter estimates. Additionally, because our hierarchical model is fit to a larger number of individuals than in previous studies, the population-level estimate is better informed by the data, making it less reliant on the prior. While hierarchical models can sometimes be more sensitive to prior misspecification, the larger sample size in this case helps mitigate this issue as the data is more informative.

Due to identifiability concerns, some VL parameters are fixed at values that are well established in the literature. We assume that the eclipse phase of newly infected cells, k_i , and the clearance rate of virus, c_i , are fixed at $k_i = 4 \text{ d}^{-1}$ and $c_i = 10 \text{ d}^{-1}$ for $i = 1, \dots, N$, respectively [5]. As outlined in Section 2.2, we parameterise the model in terms of the basic reproduction number, R_0 . Table 2 gives some estimates of R_0 for COVID-19 and Influenza as well as the dataset size (number of individuals) from the literature. None of these studies implemented hierarchical models and instead fit each individual time-series. To capture the range of values in Table 2, we assume that

Estimate (95% CI)	Number of individuals	Virus	Reference	Dataset
8.2 (NA)	25	COVID-19	[5]	NBA
11.1 (6.6, 18.5)	6	Influenza A	[2]	Other
13.51 (4.5, 45.12)	9	COVID-19	[43]	Other
14.2 (NA)	6	COVID-19	[18]	NBA

Table 2. Estimated R_0 values from published literature. Estimates and 95% CI where available of R_0 from published models. Information as to the type of viral infection and the number of individuals in the study are also provided. The dataset column indicates what dataset was of interest for that particular study, with NBA denoting a subset of our dataset and other denoting a different dataset.

$$\mu_{R_0} \sim \text{Gamma}\left(\frac{10}{3}, 3\right).$$

This choice results in a mean of 10 with a 95% quantile interval of (2.3, 23.3), providing a weakly informative prior centered near commonly reported estimates.

A meta-analysis of WHVD studies on Influenza [44] provides experimental estimates for the average period of infectiousness of an infected cell, $1/\delta$, ranges from 0.5 to 2 days

which corresponds to a removal rate of between 0.5 and 2. We assume

$$\mu_\delta \sim \text{Gamma}(26, 0.05)$$

which yields a mean rate of removal of $1.3 d^{-1}$ with a 95% quantile interval of (0.85, 1.85).

The parameter μ_ρ is difficult to assign a prior, as it has identifiability issues similar to β [5, 18]. To address this, we assume

$$\mu_\rho \sim \text{Gamma}(10, 0.3),$$

which has median $3.5 d^{-1}$ (roughly based on [5]) and a long upper tail with a 95% quantile interval of (1.1, 8.77). This distribution is deliberately weakly informative and reflects values estimated for COVID-19 in other studies [43, 45].

The remaining parameters are assigned weakly informative priors that were selected to guide the fitting process but are not taken from the literature. We assign Half-Normal priors on σ_{R_0} , σ_δ , and σ_π

$$\begin{aligned}\sigma_{R_0} &\sim \mathcal{N}_+(0, 3), \\ \sigma_\delta &\sim \mathcal{N}_+(0, 1), \\ \sigma_\rho &\sim \mathcal{N}_+(0, 3).\end{aligned}$$

The hyper-prior for σ_{R_0} and σ_ρ have a larger standard deviation compared with σ_δ as we found in our testing that a $\mathcal{N}_+(0, 1)$ over-constrained the fitted estimates which caused excessive shrinkage of the individual level parameter estimates to the population mean.

We use a non-centred parameterisation (NCP) for the individual-level parameters to enhance posterior sampling efficiency [46]. Specifically, the individual-specific parameters R_{0_i} , δ_i , and ρ_i are modelled as

$$R_{0_i} = \mu_{R_0} + \sigma_{R_0} z_{R_{0_i}}, \quad \delta_i = \mu_\delta + \sigma_\delta z_{\delta_i}, \quad \rho_i = \mu_\rho + \sigma_\rho z_{\rho_i}$$

where $z_{R_{0_i}}, z_{\delta_i}, z_{\rho_i} \sim \mathcal{N}(0, 1)$. This parameterisation facilitated more efficient posterior sampling.

The scale parameter of the measurement noise, κ , is also assigned a weakly informative prior

$$\kappa \sim \mathcal{N}_+(0, 1).$$

The priors on the infection times are also chosen to be weakly informative, where we only make the assumption that they are most likely to occur prior to the peak VL measurement,

$$t_{0_i} \sim \text{Gumbel}(-7, 3).$$

This choice results in a median time of infection (pre-peak VL) of -5.9 days. This prior assumes infection occurs most likely before peak VL but allows for post-peak infection times, which may occur in some cases due to measurement variability or delayed detection. Typical scenarios where this prior is useful is when the peak VL is a low measurement or all measurements are tightly clustered in time so it's difficult to distinguish whether the peak is early or late on in the infection. This distribution is consistent with the incubation periods of COVID-19 (pre-Omicron variant) [47] when assuming that peak infectiousness (i.e. peak VL) corresponds to symptom onset. For ease of notation we will denote the set of all hyper-parameters as

$$\phi = (\mu_{R_0}, \mu_\delta, \mu_\rho, \sigma_{R_0}, \sigma_\delta, \sigma_\rho).$$

2.7 Inference

The form of Eq. (9) suggests a Gibbs sampler that draws from the conditional distributions for each of the individuals ($i = 1, \dots, N$) and the shared parameters (ϕ, κ). However, sampling directly from the conditionals is not possible as the distributions cannot be normalised—or recognised as standard distributions—so we use a Metropolis-Hastings step within the Gibbs sampler. The conditional distributions for the individual parameters, noting that θ_i are independent of $\Theta_{-i} = \{\theta_1, \dots, \theta_{i-1}, \theta_{i+1}, \dots, \theta_N\}$ given ϕ , are given by

$$f(\theta_i | \phi, \kappa, \mathcal{D}) \propto f(\mathbf{y}_i | \theta_i, \kappa) f(\theta_i | \phi).$$

The conditional distribution for κ and ϕ is

$$f(\phi, \kappa | \Theta, \mathcal{D}) \propto f(\kappa) f(\phi) \prod_{i=1}^N f(\mathbf{y}_i | \theta_i, \kappa) f(\theta_i | \phi). \quad (15)$$

Let the current draw be $\{\Theta^{(k)}, \phi^{(k)}, \kappa^{(k)}\}$ and we use the notation $\Theta_{a:b} = \{\theta_a, \dots, \theta_b\}$ for integers a and b ($b > a$). Define the following collections

$$\begin{aligned} \psi_i^{(k+1)} &= \left\{ \Theta_{1:i}^{(k+1)}, \Theta_{i+1:N}^{(k)} \right\}, \quad i = 1, \dots, N-1, \\ \psi_N^{(k+1)} &= \left\{ \Theta_{1:N}^{(k+1)} \right\}. \end{aligned}$$

We choose a relatively simple multivariate Gaussian proposal distributions centered on the current values of the parameters being drawn, with $N+1$ separate covariance matrices per step of the method, i.e.

$$\begin{aligned} \theta'_i | \theta_i^{(k)} &\sim \mathcal{N}(\theta_i^{(k)}, \Sigma_i), \quad i = 1, \dots, N, \\ (\phi', \kappa') | (\phi^{(k)}, \kappa^{(k)}) &\sim \mathcal{N}((\phi^{(k)}, \kappa^{(k)}), \Sigma_{N+1}), \end{aligned}$$

Blocking the proposals in this way enables the subject specific proposals as well as the proposal for the shared parameters, κ and ϕ , to be tuned separately. The covariance matrices are tuned by performing a sufficiently large pilot run. Denote the PDF of the proposal distributions by $Q(\cdot | \cdot)$, where the arguments specify the particular proposal distribution being used. The acceptance probabilities for individual parameters ($i = 1, \dots, N$) are given by

$$\alpha_{1,i} = \min \left\{ \frac{f(\theta'_i | \psi_{i-1}^{(k+1)}, \phi^{(k)}, \kappa^{(k)}, \mathcal{D})}{f(\theta_i^{(k)} | \psi_{i-1}^{(k+1)}, \phi^{(k)}, \kappa^{(k)}, \mathcal{D})} \times \frac{Q(\theta_i^{(k)} | \theta'_i)}{Q(\theta'_i | \theta_i^{(k)})}, 1 \right\}, \quad (16)$$

Similarly, the acceptance probability for the shared parameters is

$$\alpha_2 = \min \left\{ \frac{f(\phi', \kappa' | \psi_N^{(k+1)}, \mathcal{D})}{f(\phi^{(k)}, \kappa^{(k)} | \psi_N^{(k+1)}, \mathcal{D})} \times \frac{Q(\phi^{(k)}, \kappa^{(k)} | \phi', \kappa')}{Q(\phi', \kappa' | \phi^{(k)}, \kappa^{(k)})}, 1 \right\}. \quad (17)$$

Note that the proposal distributions are symmetric and so the ratio of the proposal distributions in Eq. (16) and Eq. (17) are equal to 1. Algorithm 2 outlines a single step of the Metropolis-within-Gibbs sampler.

2.8 Implementation details

2.8.1 Parallelisation of the inference method

The structure of the inference algorithm and the form of the conditional distributions (Eq. (15)) allow for straightforward parallelisation. The for loop (lines 1-4 of

Algorithm 2 Single step of the Metropolis-within-Gibbs algorithm

Inputs:

- Current draw $(\Theta^{(k)}, \phi^{(k)}, \kappa^{(k)})$;
- Conditional distributions; $f(\theta_i | \phi, \kappa, \mathcal{D})$, $f(\phi, \kappa | \Theta, \mathcal{D})$;
- Transition kernels; $Q(\theta'_i | \theta_i)$ for $i = 1, \dots, N$, $Q(\phi', \kappa' | \phi, \kappa)$

- 1: **for** $i = 1, \dots, N$ **do**
- 2: Propose individual parameters $\theta'_i \sim Q(\theta'_i | \theta_i^{(k)})$.
- 3: Compute $\alpha_{1,i}$ (Eq. (16)) and accept proposal with probability $\alpha_{1,i}$.
- 4: **end for**
- 5: Propose shared parameters $\phi', \kappa' \sim Q(\phi', \kappa' | \phi^{(k)}, \kappa^{(k)})$.
- 6: Compute α_2 (Eq. (17)) and accept proposal with probability α_2 .

Algorithm 2) samples the VL model parameters θ_i independently of the other individuals given the shared parameters. This means that the sampling of the individual parameters can be parallelised across the individuals. Additionally, parallelisation can also be used when computing the acceptance probability in line 6 as the likelihood contributions from each individual in Eq. (15) (the $\mathcal{L}_i(\theta_i, \kappa)$ terms inside the product) can be computed in parallel conditional on a draw of the hyper-parameters ϕ .

2.8.2 Amortised learning of parameters for the time-shift distribution

One particular challenge with using the time-shift approach in a statistical inference framework is that computing the parameters of the distribution is itself a computationally expensive task. Each call of the likelihood requires optimisation to be carried out to determine the parameters of the time-shift distribution [17]. To overcome this performance bottleneck, we utilise a neural network (NN) to learn the parameters of the time-shift distribution, (a, b, p) , given VL model parameters, $\theta = (R_0, k, \delta, \rho, c)$. Note the removal of t_0 from the VL model parameters as the time-shift distribution does not depend on the infection time. This process is referred to as amortised optimisation [48–50] and is a common technique in machine learning to improve the efficiency of computationally complex algorithms such as MCMC [50].

We briefly describe our approach to learning the time-shift distributions here but leave full technical details to Section 3 of [S1 text](#). Let $\zeta_i = (a_i, b_i, p_i)$ denote the parameters of the time-shift distribution for some model parameters θ_i . We generate our dataset by sampling VL model parameters from a hyper-cube that encompasses our model priors. Our previous work [17] is used to determine the time-shift distribution parameters to give the paired data, $\{(\tilde{\theta}_i, \zeta_i)\}_{i=1}^n$. The time-shift distributions are checked for validity purposes since sampling on the hyper-cube does not necessarily produce feasible parameter combinations. Instead of naively sampling parameters, we check that the growth rate, $\lambda > 0$, and that 95% of the density for τ is between $[-7, 7]$. The first condition ensures that there is a non-zero probability of the infection going non-extinct before reaching the exponential growth phase. The second condition ensures that long time-shifts, typically about a half of the total viral infection time-span (in our case), are considered un-biological and that time-shifts lying outside range likely suggests an incorrect model specification or poor prior choices. The goal here is to learn a function $g : \mathbb{R}^5 \mapsto \mathbb{R}^3$ given by $g(\theta_i) = \zeta_i$ to a high degree of accuracy. The learned function will approximate the mapping from the VL model parameters to the time-shift parameters without the need to perform complex numerical routines. Replacing the numerical routine with this learned function makes the runtime to find the parameters approximately 200× faster.

2.8.3 Software

All analyses in this paper were implemented in the Julia programming language [41], which provides seamless integration of model specification, automatic differentiation, and inference within a single environment. For solving ordinary differential equations, we used the high-performance solvers provided by OrdinaryDiffEq.jl [51]. The neural network used to approximate the time-shift distributions was implemented and trained using Flux.jl [52]. Automatic differentiation was performed using ForwardDiff.jl [42].

2.9 Datasets

In this analysis, we use two datasets: a published dataset of COVID-19 VL measurements collected during the 2020-2021 NBA season restart, and a synthetic dataset designed to resemble the NBA dataset for method validation. The synthetic dataset serves as a controlled setting with frequent, low-noise observations and known parameters. It consists of $N = 100$ individuals and is generated using our prior model for the hyperparameters ϕ . The full data generation process is detailed in Section 2.9.1, and the simulated cohort is shown in Fig. 3A.

The NBA published COVID-19 monitoring data on players and staff during the 2019-2020 season restart [4, 6]. Individuals were regularly tested for SARS-CoV-2 from mid-2020 to the season’s end, yielding log-transformed viral load measurements relative to peak VL. Other studies using mechanistic models [5, 18] had to selectively include individuals with frequent pre- and post-peak observations; in our analysis we fit to a much larger set of individuals, many with much poorer data, simultaneously. There are 241 individuals in total (68 in [6] and 173 in [4]) but some of these time-series are quite noisy so we performed some pre-processing before fitting. Following the approach of Zitzmann et al. [5] we excluded individuals with viral loads detected outside a 14-day window around peak VL, as our model does not account for complex behaviours like long-term infections.

The limit of detection (LOD) in the NBA dataset is 2.658 log copies/mL and frequent testing and individuals experiencing only single infections resulted in many observations (i.e. some individuals having 80% LOD observations) at this threshold for each individual. Since it is most likely that individuals are only actually positive for some number of days pre/post the time where they have above LOD observations, we truncated the time series, retaining only the LOD measurements such that above-threshold observations remained between them. In some cases, multiple values below the LOD occur before another measurement slightly above the detection limit which complicates fitting. To address this, we further truncated time series at three consecutive threshold observations [6]. Finally, there were some short time-series—i.e. less than 2 observations above the LOD—and these were excluded. After filtering our dataset contains 163 of the original 241 timeseries. Note that we use the same post-processing procedure and LOD for the synthetic dataset. The NBA data is shown in Fig. 3B alongside our simulated cohort in panel Fig. 3A. The NBA data (Fig. 3B) exhibits visibly higher variance across the entire time horizon compared to the simulated dataset (Fig. 3A). This is primarily because the synthetic data were deliberately generated with lower noise to enable more controlled validation of our method.

Our hierarchical model shares information from individuals with high information to improve estimates for those with sparse data, a process known as partial pooling [46, Chapter 5]. Previous analyses of this dataset [4–6, 12] used deterministic models [5, 12] or piecewise linear functions [4, 6, 12], whereas our model explicitly accounts for stochasticity in VL trajectories. Since we include individuals with both high and low information, direct parameter comparisons to Zitzmann et al. [5] are not possible. However, we can compare our R_0 estimates to their results and those from

other SARS-CoV-2 studies [53] as well as other respiratory illnesses [31, 53]. Additionally, we compare predicted VL trajectories to those in Zitzmann et al. [5]. Phenomenological models [4, 11] estimate parameters based on piecewise linear models, which are not directly comparable to our mechanistic approach, but our model can estimate the same summary statistics as phenomenological models while also inferring biological quantities like R_0 .

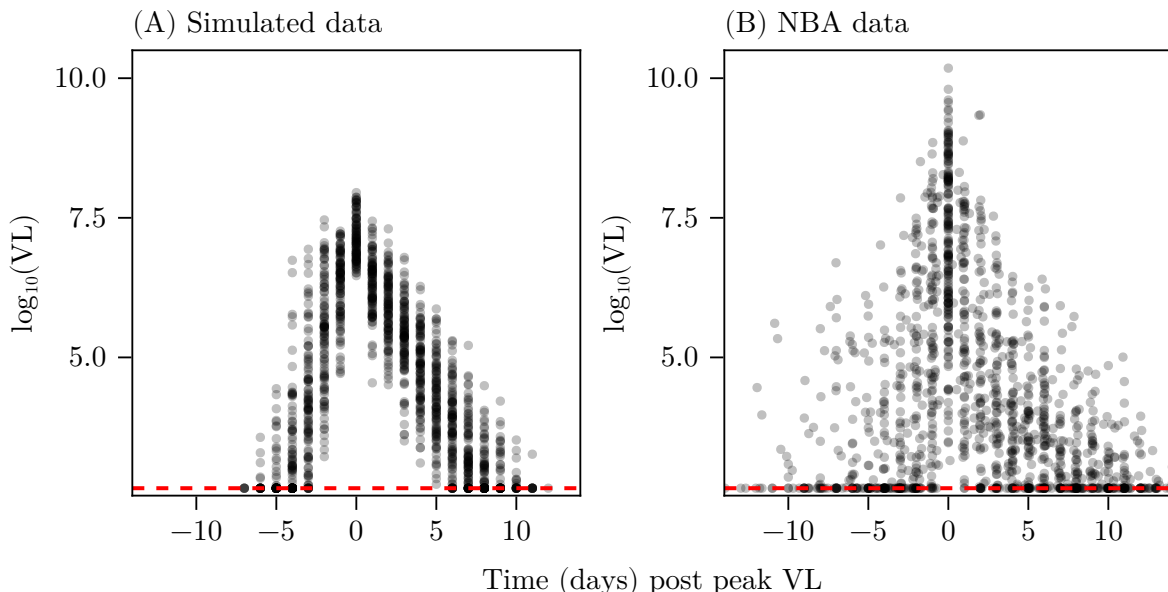


Fig 3. Scatter plots of the simulated and NBA datasets. Panel (a): the synthetic VL dataset generated according to the process in Section 2.9.1. Panel (b): the NBA VL dataset for the 2020-2021 seasons. In each panel an individual data point corresponds to a single measurement for a single individual. Points are shown as semi-transparent to approximate the “density” of points—highlighting outliers in panel (b). The red dashed line indicates the limit of detection.

2.9.1 Generating synthetic data

We construct our synthetic dataset by initially sampling VL model parameters from the prior setup as outlined in Section 2.6. This requires fixing the shared parameters and sampling individual parameters from priors. The means of the shared parameters ($\mu_{R_0}, \mu_\delta, \mu_\rho$) are chosen to be in agreement with previous estimates [5]. The scale parameters ($\sigma_{R_0}, \sigma_\delta, \sigma_\rho$) were arbitrarily selected based on comparing the simulations to the NBA dataset. The measurement noise parameter κ was chosen to be 0.5 to reflect a reasonable amount of noise in the measured VL’s but still a “low noise” situation to assess the model in an ideal scenario. The values of all shared parameters are given in Table 3.

Model parameters θ_i are sampled for each individual from the priors assuming the values of the hyper-parameters in Table 3. Infection times are then drawn from the prior and then a time-series for each individual is simulated by running Algorithm 1. The variability in the priors causes a wide range of growth and decline rates as well as peak \log -VL values which can cause unrealistic scenarios such as virus never being eliminated. In order to ensure we generate realistic data, we simulate under a rejection

Parameter	Value
μ_{R_0}	8
σ_{R_0}	0.5
μ_δ	1.3
σ_δ	0.15
μ_ρ	3
σ_ρ	0.25
κ	0.5

Table 3. The values of the shared parameters used to generate the synthetic dataset.

framework whereby we accept a simulation if an individual has peak log-VL between 5 and 10 (visually consistent with the range in the peak log-VL’s in the NBA dataset) and a corresponding peak infection time of between 4 and 9 days post-infection. We also require that the decline rate is consistent with a typical acute infection and so we require the log-VL to be less than 4.5 at the end of the observation period (21 days post-infection). This condition ensures we do not have long-tails which are biologically invalid (i.e. no viral clearance). As in the NBA data, we assume a LOD of 2.658 log copies/mL, processing these as outlined in Section 2.9. Overall, the simulated dataset constitutes an idealised scenario where individuals have multiple observations in both the growth and decline phases.

3 Results

We apply our method to the two datasets outlined in Section 2.9. The initial exploration of the model fit to the synthetic dataset enables us to demonstrate the ability of the algorithm to produce accurate fits to the data for each individual in a situation where we know the true parameter values. The NBA dataset is used to demonstrate the utility of the method in a real-world scenario where the true parameter values are unknown.

All simulations and models were implemented in Julia [41] and run on a 2021 MacBook Pro with an M1 chip and 16 GB of RAM. Likelihood computations were parallelised across 4 high-performance CPU cores, as described in Section 2.8. A pilot run was used to tune the proposal distributions for both individual and shared parameters. Following this, we initialised four chains from perturbed versions of the parameters used to generate the synthetic data, to assess the robustness of the sampler to initial conditions. Each chain was run sequentially for 100,000 iterations, with the first 10,000 discarded as burn-in. The run times for the NBA dataset (the larger of the two datasets) took approximately 10 minutes per chain for a total runtime of approximately 45 minutes.

Trace plots for all shared parameters and a subset of individual parameters were visually inspected for divergences and showed no signs of poor mixing across the chains for both analyses. All parameters had $\hat{R} \leq 1.01$, indicating good within- and between-chain mixing [54], and effective sample sizes exceeded 1000 across both datasets. The acceptance rates were approximately 0.30 and 0.4 for the individual (averaged across groups) and shared parameters, respectively, both within the expected range for well-tuned random walk Metropolis proposals [55].

3.1 Simulation study

In this section, we present the inference results for the simulated dataset. The marginal distributions of the shared parameters, ϕ and κ , are shown in Fig. 4, with prior

distributions in yellow and posterior distributions in blue. True values, shown by the vertical dashed black lines, are computed from the sampled individual parameters since naively using the true parameters (i.e. Table 3) would be incorrect as our post-processing steps—like censoring observations—change how these are actually distributed. In what follows we refer to these estimated parameters as the “ground truth parameters”. For all parameters we observe substantial shifts from prior to posterior, indicating the influence of the data on the inference. All posteriors centered close to the ground truth values, demonstrating the method’s strength in estimating them.

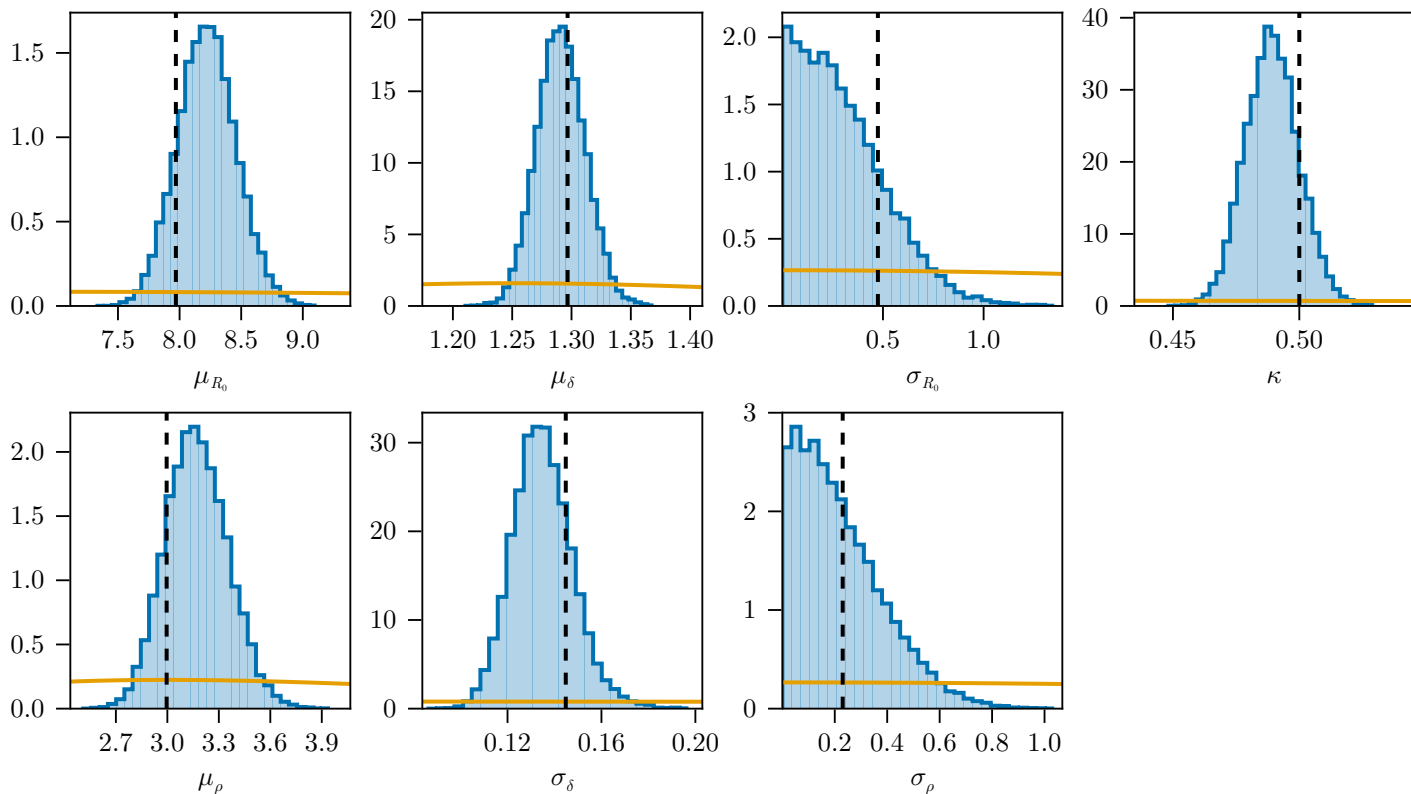


Fig 4. Density plots for the marginal distributions of the shared parameters (hyper-parameters and the scale of the measurement noise). Prior distributions are given by the orange lines and posteriors are represented by the blue histograms. The values indicated by the vertical dashed black lines are the true estimates of the parameters computed from the parameters used to simulate the dataset.

Fig. 5 shows the posterior predictive distributions for R_0 , δ , and ρ . These are obtained by using the posterior sampled hyper parameters and evaluating the normal model, i.e. for a draw $(\mu_{R_0}, \sigma_{R_0})$, we sample $R_0^* \sim \mathcal{N}(\mu_{R_0}, \sigma_{R_0})$, and similarly for δ and ρ . The posterior predictive distributions represent the distribution of parameters that could be drawn if we sampled a new set of parameters. We can see from the posterior predictive distribution for all parameters that the model is able to appropriately capture the range of simulated parameters.

The difference between the posterior sampled parameters and the true values is shown in Fig. 6. Each subplot represents a different parameter, with the horizontal black line indicating a difference of 0 (strong parameter recovery). Intervals are

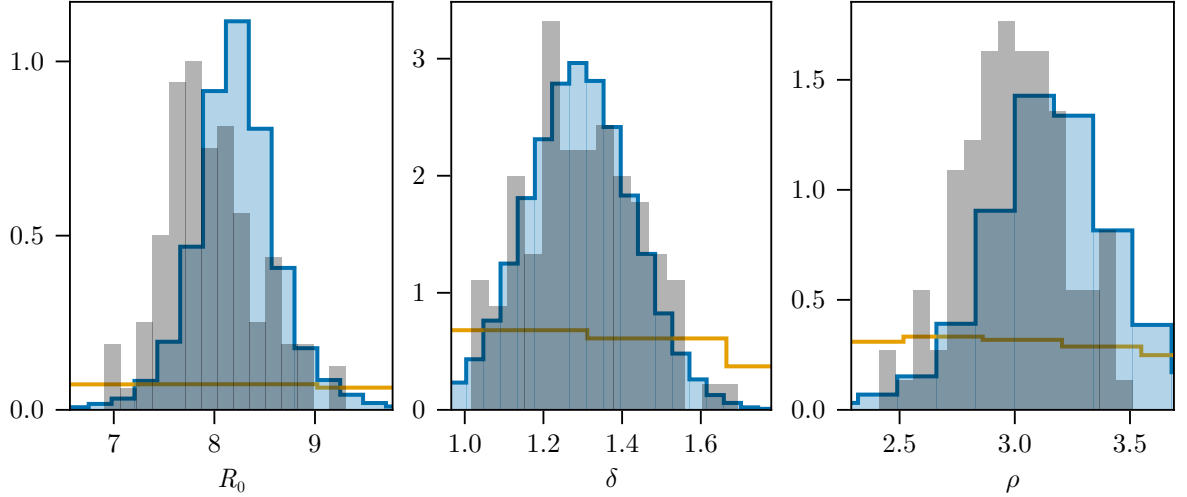


Fig 5. Posterior Predictive Distributions for R_0 , δ , and ρ . The blue histograms show the posterior predictive distributions, while the grey shaded bars indicate the true parameter values used in the simulation. The grey histogram is noisy as there are only 100 parameter values sampled. The orange lines represent the prior predictive distributions. For clarity, we have zoomed in on the sampled values.

coloured red if 0 is not within the 95% credible interval of the difference, and individual IDs are listed for ease of reference. In Fig. 6C, the true production rate, ρ , is contained within the 95% interval for all individuals except for individuals 1, 33 and 51. Fig. 6D shows that the infection times are generally well-estimated, with only 8 individuals not containing 0. This behaviour is expected due to the weakly informative priors on infection times and the censoring of data below the limit of detection that contributes to the slight misestimations. In the worst case, the infection times are off by up to 2 days. Fig. 6B shows 6 individuals where the interval for the difference in δ does not contain 0, suggesting these may be outliers. Similarly, in Fig 6A, 7 individuals have posteriors for R_0 that do not contain 0. These discrepancies are likely a result of pooling in our model, which will be further explored in the posterior predictive analysis shown next. Overall, even in cases where a parameter is slightly misestimated, the model still recovers the other parameters accurately.

Fig. 7 shows the posterior predictive fits for the synthetic dataset for the 22 individuals where a parameter was outside the 95% interval of the differences in Fig. 6. In all cases, the modelled trajectories track the observed data well. Cases where δ appears to be misestimated often coincide with visually noisier data in the decline phase (e.g., IDs 31, 44, 52, 59, 77, and 81). In these instances, most observations lie close to the median trajectory, with discrepancies likely arising due to noise in the data rather than model misspecification.

In addition to the trajectories and estimated parameters, by its construction, our model can estimate the posterior predictive time-shift for individuals. Here we show only a single individual as the other results all reflect the same prior predictive time-shift samples (orange) and similar posterior predictive curves (in blue). The time-shifts are shown in Fig. 8 where we see that the prior predictive time-shift distributions are quite wide and highly varied. Some of the density functions have large amounts of density concentrated above 1-2 days and have long tails (in both directions).

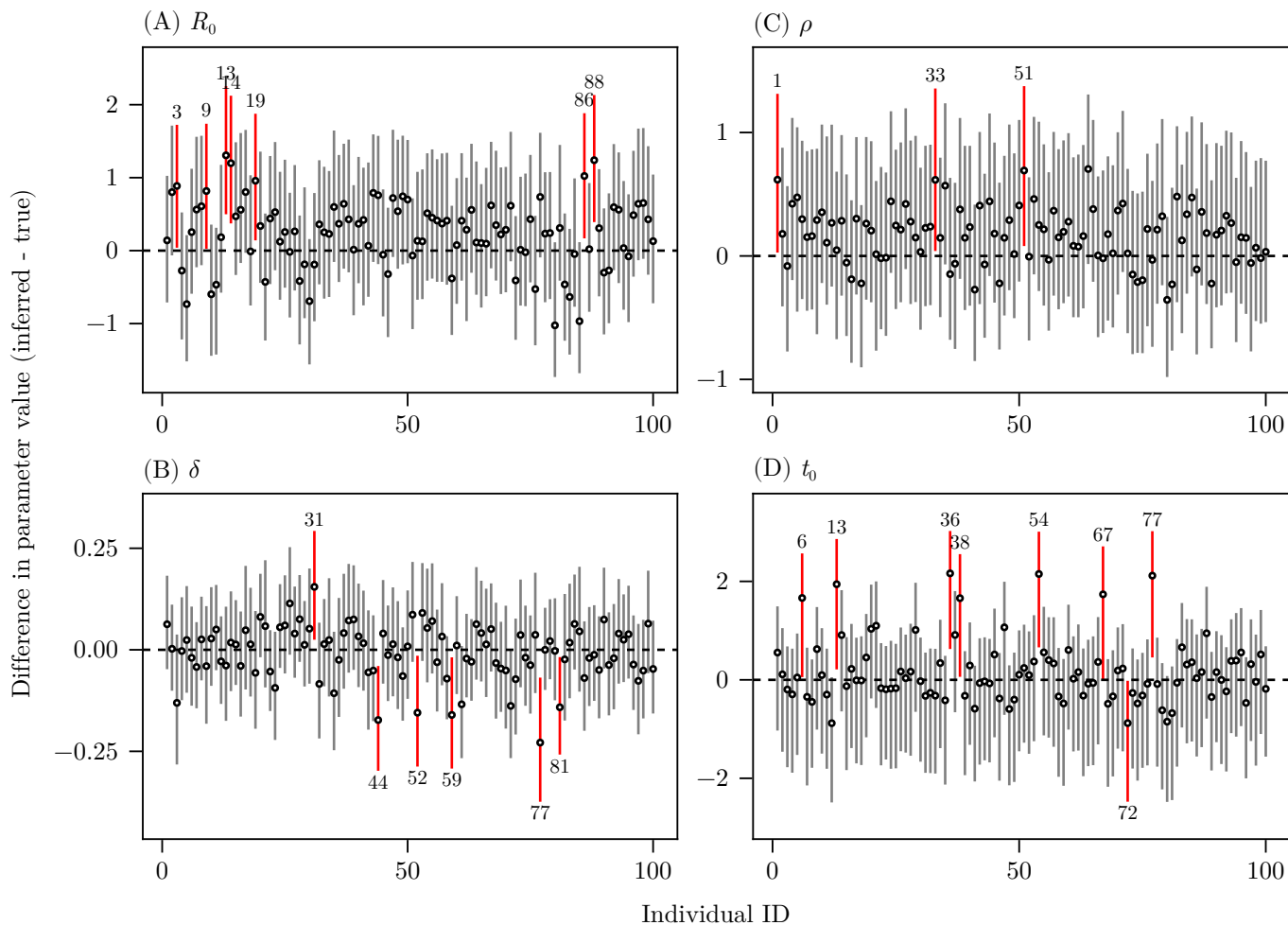


Fig 6. Interval plot showing the 95% intervals of the difference between posterior parameters and the true values for the simulated dataset. Panels (A)-(D) show the 95% interval of the difference between the posterior parameters and the true individual parameters. Parameter of interest is listed in the title of each subplot. The horizontal black dashed lines indicate a difference of 0. The white circles indicate the median difference. Individuals with 0 not in the 95% intervals have their intervals coloured in red and their ID is listed above or below the interval (depending on direction of difference).

Contrasting this, the posterior predictive time-shift distributions (blue) are more concentrated, with the distributions roughly resembling one another besides the variation arising from the posterior sampled parameters themselves.

3.2 NBA study

In the main text we report only the marginal posteriors for the shared parameters and posterior predictive VL trajectories for select individuals. The marginal posteriors for the shared parameters are shown in Fig. 9. We see that there is large movement in the distributions from the prior (orange) to the posteriors (blue) for all parameters besides

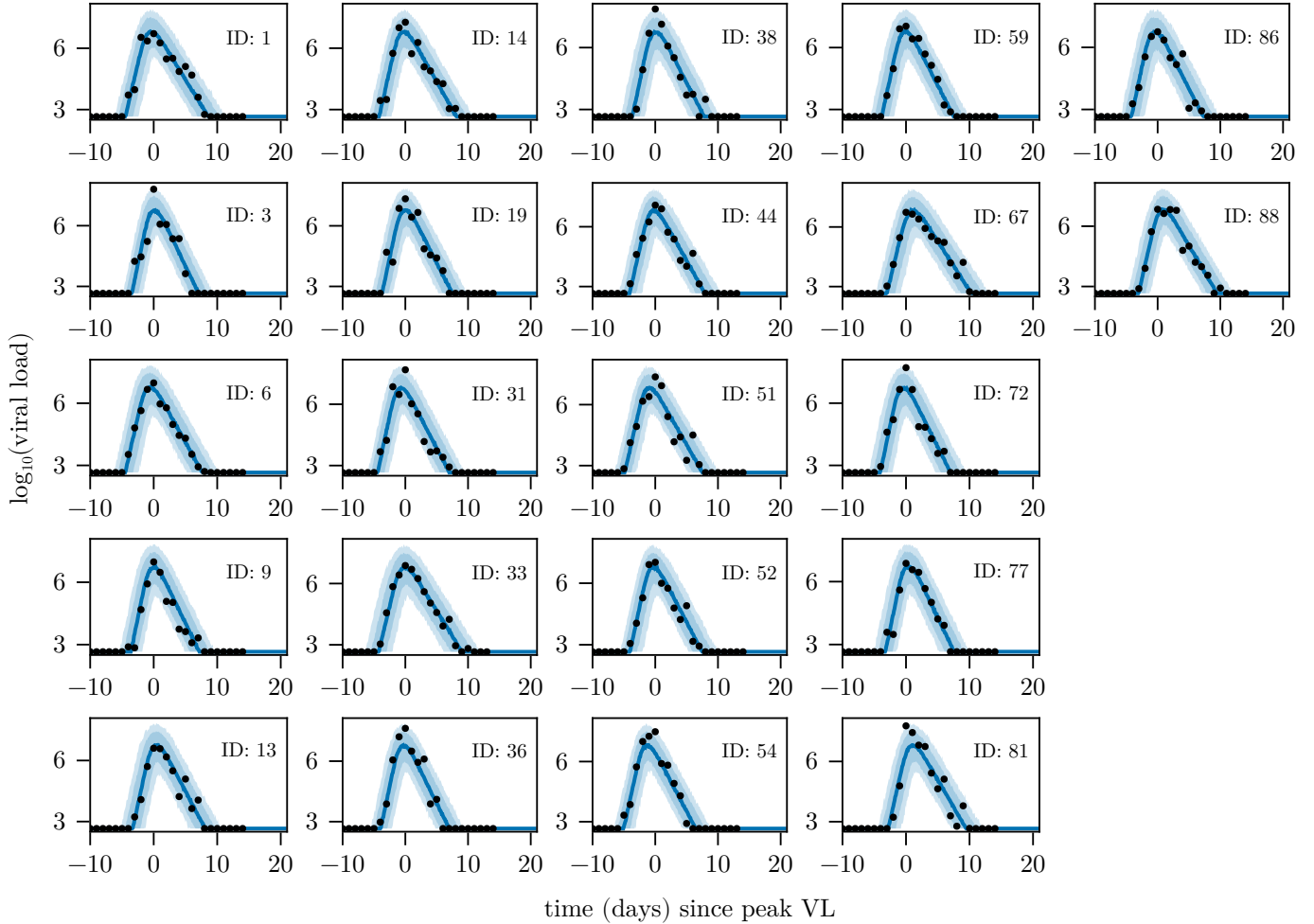


Fig 7. Posterior predictive fits for the synthetic dataset. Posterior predictive VL trajectories for individuals with 0 not in one of the intervals in Fig. 6. Solid lines represent the median of the posterior predictive fits and the shaded regions represent the 80% and 95% prediction intervals. Black dots indicate observed data. All subplots show the same time period $[-10, 21]$.

σ_{R_0} . This is not surprising since the individual parameters R_0 , δ , and ρ values trade-off with one another and with less data in the growth phase, this can cause the related hyper-parameters to be weakly identifiable when inferred jointly. The model appears to be able to estimate all parameters including the measurement noise κ . Our estimates for μ_{R_0} —and by extension—the individual R_0 's are consistent with the results in Table 2. It should be noted that compared to Zitzmann et al. [5] our population estimate is larger 15.3 compared with 8.2. One possible reason for this is that our model accounts for the probability of extinction during the early phase which is non-negligible when assuming the infection is initiated by a single cell in the eclipse phase. This potentially biases the results in [5] downwards. Our R_0 estimates are consistent with the value of 14.2 reported in Germano et al. [18] from their stochastic model (which also accounts for immune responses). Our population estimate for μ_ρ is 6.57 which is larger than the

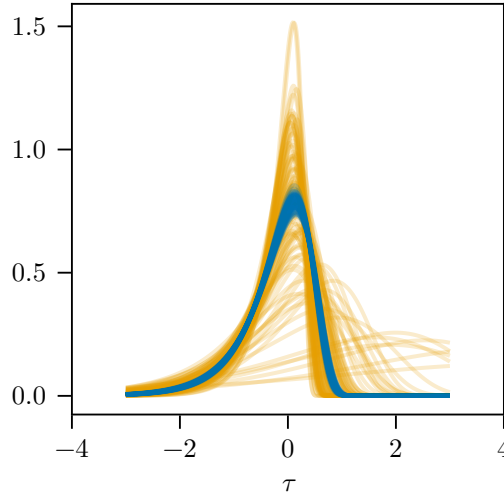


Fig 8. Time-shift posterior predictive distributions. Posterior predictive (blue) and prior predictive (orange) time-shifts for a single individual in the synthetic dataset.

estimate of 3.07 in [5]. We infer the population mean rate of removal for infectious cells to be 1.27 as in Zitzmann et al. [5]. There are several possible reasons for the difference in the estimates of R_0 and ρ . The first being that, as our model is stochastic, larger values of the parameters are required to ensure that the model overcomes extinction than what would be estimated by a deterministic model. We are also fitting to a much larger number of individuals (163 vs 25) including those that are unvaccinated and have limited data during the growth and decline phases. Additionally, we account for the LOD in our model and make no assumptions as to the time from infection to peak instead allowing our model to infer the infection time.

Fig. 10 shows the posterior predictive VL fits (blue) for a subset of individuals in the NBA dataset. The first row of Fig. 10 corresponds to data for four individuals also analysed in Zitzmann et al. [5] alongside their estimated VL trajectories (orange crosses). We see strong agreement between our model and the Zitzmann et al. [5] model, with our median predictions closely tracking their estimated trajectories.

The second row of plots corresponds to individuals (visually) selected for having limited data in either the pre- or post-peak phase. The posterior predictive trajectories generally track the observed data well, though some interesting features emerge for individuals 2987 and 10981. For these two, the light-blue prediction intervals indicate the possibility of earlier infection times. Given the limited data during the increasing or declining phases of their infections, this behaviour is plausible.

4 Discussion

We have presented a novel method for fitting mechanistic within-host viral dynamics models that explicitly account for process noise, providing a more realistic representation of viral load (VL) trajectories. Our approach leverages the concept of a random time-shift—first introduced in Barbour et al. [16] and later developed into a practical tool in Morris et al. [17]—to capture the effects of stochasticity in the WHVDs. A key contribution of this work is demonstrating how the time-shift distributions can be directly incorporated into the likelihood function, allowing stochasticity to be modelled

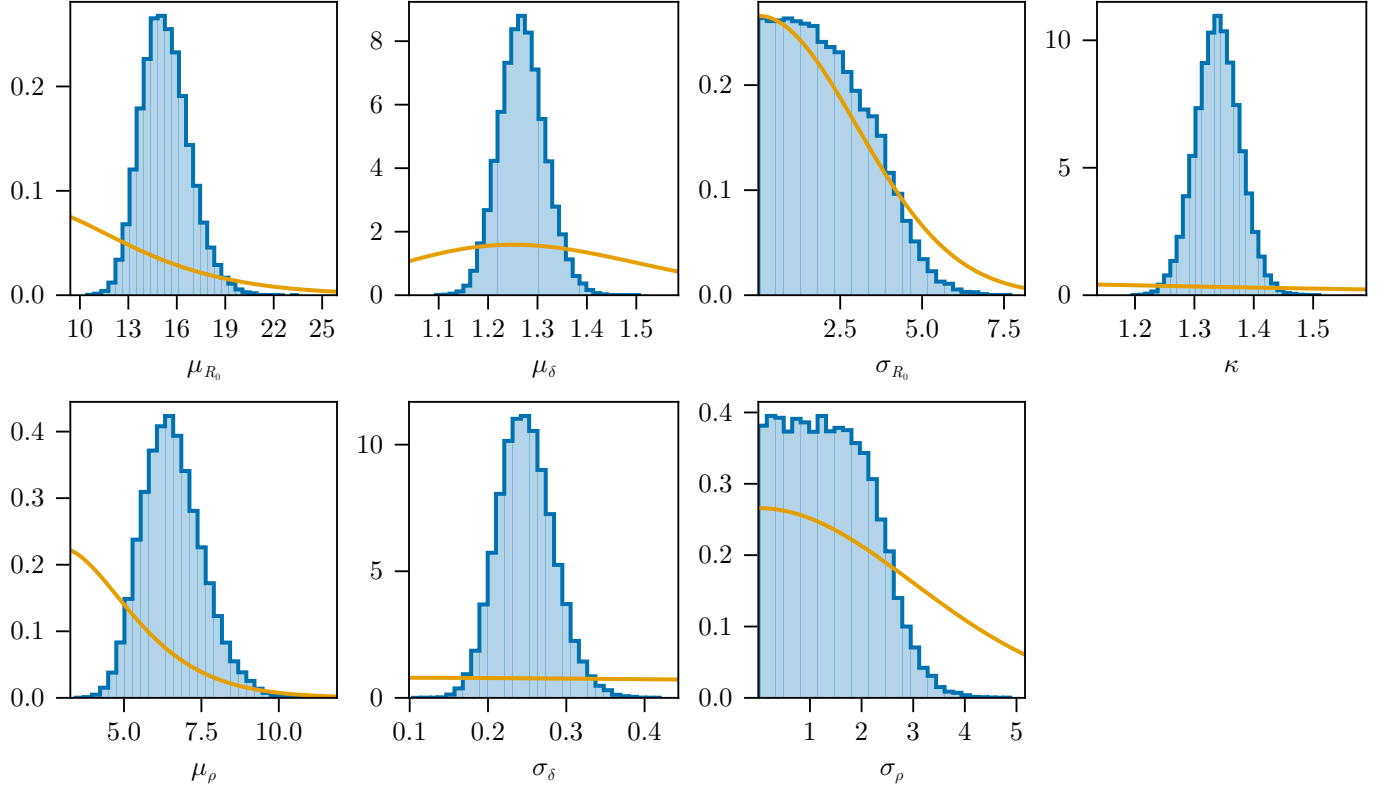


Fig 9. Density plots for the marginal distributions of the shared parameters (hyper-parameters and the scale of the measurement noise) for the NBA model fit. Prior distributions are indicated in orange and posteriors are given by the blue histograms.

without the need for computationally expensive stochastic simulations, for example using Gillespie’s algorithm [22] or tau-leaping [23]. This enables efficient inference, making it feasible to fit the model to large datasets using a hierarchical framework. Our approach can be viewed as a hybrid method, combining the interpretability and tractability of deterministic models while capturing key elements of stochastic modelling, offering a middle ground between fully stochastic simulation and purely deterministic fitting.

Hierarchical approaches have been widely used in phenomenological studies of WHVDs [6, 11], but to our knowledge, no stochastic WHVD models have incorporated hierarchical structures. The existing approaches fall into two main categories: simpler parametric models, such as piecewise linear functions [4, 6, 11], and mechanistic models that assume deterministic dynamics [5, 12, 25, 38]. Parametric models offer computational advantages, as their likelihoods are easier to evaluate and they integrate well with probabilistic programming frameworks like Stan [56]. However, they primarily describe viral dynamics in terms of slope parameters (for growth and decline) and a hinge point (for peak VL), limiting their ability to extract biologically meaningful quantities like R_0 and production rates ρ . Mechanistic models, in contrast, provide a more realistic representation of infection dynamics but are computationally expensive due to the need to repeatedly solve ODEs. This challenge is especially pronounced in

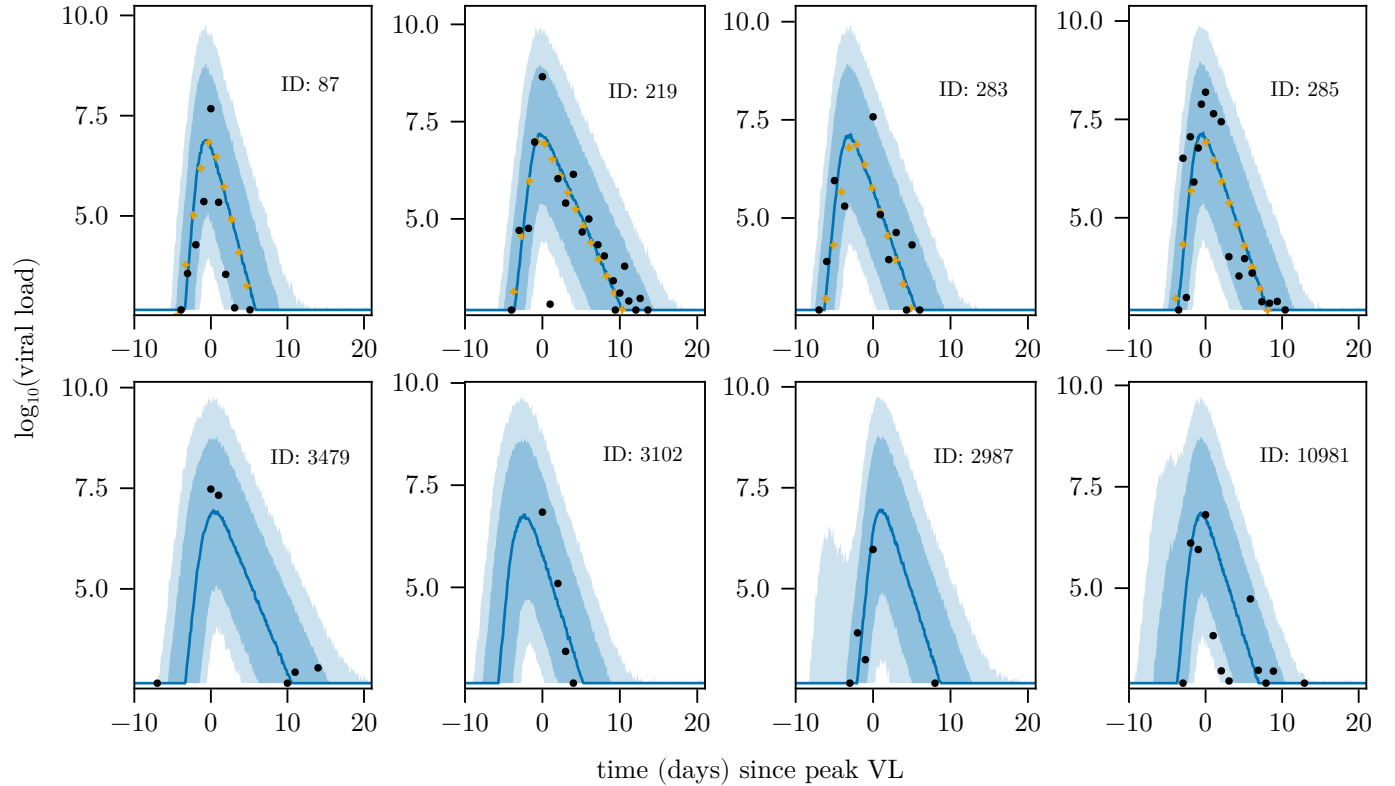


Fig 10. Posterior predictive fits for a subset of individuals from the NBA dataset. The first row of plots corresponds to a subset of individuals also presented in Zitzmann et al. [5] for comparison purposes. The second row corresponds to individuals not studied in Zitzmann et al. [5], but that have sparse data (which were selected by visual inspection). The observations for each individual are shown in black. The solid lines represent the median of the posterior predictive fits and the shaded regions represent the 80% and 95% prediction intervals. The orange crosses in the first row of plots indicate the deterministic VL trajectories estimated in [5]. All subplots show the same time period $[-10, 21]$.

Bayesian inference for large datasets. Moreover, parameter identifiability can become a major concern in this context, particularly when biological parameters influence the VL in overlapping ways (i.e. the relationship between R_0 , the viral production rate, the infection time and initial conditions) [5, 25]. While some hybrid stochastic-deterministic models [18, 57, 58] have been developed, they remain computationally demanding and have not been widely applied to multi-individual VL kinetics studies. Our method addresses these limitations by introducing stochasticity directly into the model formulation, capturing process noise without the need for costly stochastic simulations. This ensures that parameters are not artificially inflated while maintaining computational efficiency.

We have adopted the simplest viral dynamics model for this work due to parameter identifiability concerns, but the method can easily be applied to other suitable models. These models must satisfy the conditions required for applying the time-shift approximation [16, 17], which many biological systems with large populations naturally

fulfill [17, 59, 60]. The main constraint beyond the large population assumption lies in data availability during the pre-exponential growth phase. Systems where early-time dynamics are critical to macroscopic outcomes but where direct observations are limited—such as other within-host models—are particularly well suited for this approach. Examples include the innate response model used in Zitzmann et al. [5] and more complex models, such as those examining the role of MUC1 in reducing influenza severity [14]. Conversely, these conditions also define when our method may not be the most appropriate. In cases where high-quality early-growth-phase data is available, exact stochastic methods may be preferable. Epidemic outbreak data, for instance, typically includes detailed observations during the initial growth phase when cases are few and monitoring efforts are robust, making alternative approaches more suitable.

The primary limitation of our method is its complexity compared to simpler approaches in the literature that leverage standard packages like Stan [56]. Our framework integrates multiple techniques—neural networks, random time-shift computations, Laplace approximations, and numerical solvers—to fit the model. The neural network plays a critical role in enabling the time-shift approximation by learning a smooth mapping from model parameters to the parameters of the time-shift distribution, effectively circumventing the need for expensive optimisation routines during likelihood evaluation. This learned surrogate is then embedded directly within the likelihood, facilitating fast and efficient likelihood computations. This complexity means the method is not a black box and requires expertise to debug. If performance issues arise, such as MCMC convergence problems, identifying the source of the issue within the pipeline can be challenging.

Increased method complexity often comes with computational challenges, akin to the trade-offs between importance sampling in particle filters and bootstrap filtering methods [61, 62]. To mitigate these issues, we have structured the method into several modular and easily testable steps. The two main approximations—using a neural network to learn time-shift distribution parameters and employing Laplace approximations—can both be replaced with exact computations (at the cost of efficiency) for validation. We recommend validating each component separately before applying the full framework. This includes ensuring that the neural network generalizes well beyond its training set, verifying the accuracy of time-shift distributions (e.g., by comparing against simulations from the stochastic model [17]), and using Laplace approximations only when justified (e.g., for normally distributed observation processes). Profile likelihoods can further confirm that the method accurately captures the shape of the exact likelihood, as demonstrated in Section 4 of [S1 text](#).

Another consideration is that the branching process results for each model must be computed from scratch. Since time-shift distributions are model-specific, they must be re-derived, using the framework from Morris et al. [17]. Our previous work [17] provides a package for computing the time-shift distributions given the branching process results. Additionally, the neural network must be redesigned and retrained for any new VL kinetics model as the underlying branching process structure is altered. While these challenges are not insurmountable, they are important factors when deciding whether to use this approach. However, our work here provides a general template for implementation making it substantially easier to extend the method to other models going forward.

A key advantage of our approach is its ability to model heterogeneity in viral trajectories, which is particularly relevant when initial infections involve a small number of cells. In such cases, accounting for the probability of early extinction may be important, as the likelihood of extinction is higher and could influence parameter estimates if unaccounted for. Beyond within-host modelling, incorporating stochasticity also has implications for between-host transmission studies [63–66]. Small variations in

VL trajectories can influence an individual’s infectiousness, affecting transmission dynamics in settings like household studies [37, 67, 68]. A more realistic representation of within-host variability could lead to improved estimates of key epidemiological parameters, which is an area of ongoing research.

This paper introduces a methodological advance for working with within-host viral dynamics (WHVDs), addressing a complex and increasingly important class of inference problems. Rather than proposing a new model, we focus on developing computational tools that enable efficient Bayesian inference for existing stochastic VL kinetics models. Our interdisciplinary approach—combining applied mathematics, machine learning, and computational statistics—makes it feasible to fit these models to large datasets using biologically motivated, mechanistic, models. By leveraging modern computational techniques, we present a flexible framework that can accommodate the intricacies of viral dynamics and scale efficiently. A key enabler of this work is the use of the Julia programming language [41], which allows for seamless integration of model specification, automatic differentiation, and inference within a single environment. This capability makes it possible to conduct complex analyses on local hardware, reducing the reliance on dedicated high-performance computing clusters. Overall, the methods introduced here offer a powerful toolset for advancing the study of WHVDs and supporting future research into more realistic and scalable modelling frameworks.

Supporting information

The following is the supporting information for the main text. It has been slightly adjusted to allow inclusion in a single preprint containing all materials.

S1 text

1. The deterministic approximation

Let $\mathbf{x}(t) = K^{-1}\mathbf{X}(t)$ denote the density process of the CTMC $\{\mathbf{X}(t), t \geq t_0\}$. Then reading down column 2 of Table 1 in the main text, and provided $\mathbf{a} + \mathbf{l} \in \mathcal{S}$ where \mathcal{S} is the state space of the CTMC, \mathbf{a} is the current state and \mathbf{l} represents the jumps of the process, then the (positive) transition rates can be expressed in terms of the following functions

$$r^{(K)}(\mathbf{a}, \mathbf{a} + \mathbf{l}) = \begin{cases} K\alpha sv, & \text{if } \mathbf{l} = (-1, 1, 0, 0), \\ Kke, & \text{if } \mathbf{l} = (0, -1, 1, 0), \\ K\delta i, & \text{if } \mathbf{l} = (0, 0, -1, 0), \\ K\rho i, & \text{if } \mathbf{l} = (0, 0, 0, 1), \\ Kcv, & \text{if } \mathbf{l} = (0, 0, 0, -1). \end{cases} \quad (18)$$

Since the rates can be expressed in this form (referred to as “density dependent”), by Theorem 3.1 of [35], as $K \rightarrow \infty$ the process $\mathbf{x}(t)$ converges to a deterministic process $\mathbf{x}_d(t)$ uniformly in probability over finite time intervals provided $\mathbf{x}_d(0) = K^{-1}\mathbf{X}(0)$. Letting

$$\mathbf{H}(\mathbf{x}_d(t)) = \sum_{\mathbf{l}} \mathbf{l} r(\mathbf{a}, \mathbf{a} + \mathbf{l}),$$

where $r(\mathbf{a}, \mathbf{a} + \mathbf{l}) = K^{-1}r^{(K)}(\mathbf{a}, \mathbf{a} + \mathbf{l})$, then the system of ODEs governing the deterministic approximation (Eq. 2 in the main text) is given by

$$\frac{d\mathbf{x}_d(t)}{dt} = \mathbf{H}(\mathbf{x}_d(t)). \quad (19)$$

2. Branching process results

Considering the early stages of infection within a host, the number of target cells, S , is approximately constant, i.e. $S \approx S_0$ and hence the rates in Table 1 of the main text are linear. The BPA then tracks the evolution of the state vector $\mathbf{X}_b(t) = (E, I, V)$ and the change in event and corresponding rates are given in Table 4.

$\Delta \mathbf{X}$	Rate
$(1, 0, 0)$	$\beta S_0 V$
$(-1, 1, 0)$	kE
$(0, -1, 0)$	δI
$(0, 0, 1)$	ρI
$(0, 0, -1)$	cV

Table 4. Change in state and rates for the BPA to the *TCL* model.

To apply the method in [17], we must identify the constant terms from the progeny generating functions which are defined as

$$f_i(\mathbf{s}) = \sum_{\mathbf{k}} p_i(\mathbf{k}) \prod_{j=1}^m s_j^{k_j}, \quad \mathbf{s} \in [0, 1]^m$$

where $p_i(\mathbf{k})$ is the probability of an individual of type i having $\mathbf{k} = (k_1, \dots, k_m)$ offspring of each type [17]. Let $\beta^* = \beta S_0$, then for the *TCL* model

$$\begin{aligned} f_1(\mathbf{s}) &= \frac{k}{k} s_2 = s_2 \\ f_2(\mathbf{s}) &= \frac{\delta + \rho s_2 s_3}{\delta + \rho} \\ f_3(\mathbf{s}) &= \frac{c + \beta^* s_1 s_3}{c + \beta^*}. \end{aligned}$$

The non-zero constants (see [17] for details) needed for the time-shift computations are

$$\alpha_{12} = k, \quad \beta_{223} = \rho, \quad \beta_{313} = \beta^*.$$

The probability of ultimate extinction q^* is determined by solving for the minimal non-negative solution of the following system [69]

$$f_i(\mathbf{q}) = q_i \text{ for } i = 1, 2, 3$$

where the $f_i(\mathbf{q})$ are the progeny generating functions. Making the substitution and rearranging the system yields the following system of equations

$$\rho(c + \beta)q_3^2 - (c\delta + \rho\beta)q_3 + c(\delta + \rho) = 0 \tag{20}$$

$$q_1 = \frac{\delta}{\delta + \rho - \rho q_3} \tag{21}$$

$$q_2 = q_1. \tag{22}$$

Since Eq. (20) is quadratic and only in terms of q_3 , this can be solved analytically and the remaining probabilities determined by substitution.

3. Neural network architecture and details

When generating the training data, we follow the process outlined in Section 2.8.2 of the main text. One key detail from an implementation perspective is that we also standardise the inputs (model parameters) and the outputs (time-shift parameters) using standard scaling (i.e. subtract the sample mean for each parameter and divide by the sample variance). In the context of training NN’s, this standardisation has the effect of drastically improving the performance and convergence behaviour of optimisers like Adam. We utilise a simple NN with the following architecture:

1. Input layer: 3 neurons (the free parameters of the VL model) with ReLU activation
2. Hidden layer: 64 neurons with ReLU activation
3. Output layer: 3 neurons (the parameters of the time-shift distribution) with soft-plus activation

The input and hidden layer both use the rectified linear unit (ReLU) activation functions. The first of which acts to standardise the input data and then in the output layer we use the soft-plus activation function to ensure non-negativity in the GG parameters. We consider mean-squared-error (MSE) as the loss function to be optimised as this performed well in testing and all the output parameters for the surrogate distribution are on the same scale. Let

$$\mathcal{A} = \{(\boldsymbol{\theta}_i, \zeta_i)\}_{i=1}^{n_{\text{train}}} \quad \text{and} \quad \mathcal{B} = \{(\boldsymbol{\theta}_i, \zeta_i)\}_{i=1}^{n_{\text{test}}}$$

denote the training and validation sets respectively. Let $\mathbb{M}_{\Psi}(\boldsymbol{\theta})$ denote the current NN model—where we have collected the NN model parameters into Ψ —evaluated at mechanistic model parameters $\boldsymbol{\theta}$ which returns the surrogate distribution parameters. Define $\mathbb{M}(\boldsymbol{\theta})_j$ as the j th element of this (i.e. the estimated surrogate distribution parameter using the NN), then the loss is given by

$$L(\Psi) = \sum_{i=1}^{n_{\text{train}}} \sum_{j=1}^3 (\mathbb{M}_{\Psi}(\boldsymbol{\theta}_i)_j - \zeta_j)^2. \quad (23)$$

We use the ADAM optimiser with defaults as provided by the Julia package Flux.jl. Additionally to improve the generalisability of the model, we perform early stopping. Early stopping uses the validation set and we stop training the model if there is no improvement in the loss (calculated in the same way as the loss in Eq. (23)) on the validation set after 30 epochs. The model is completely implemented and trained in Julia on a CPU (to simplify dissemination of codes) using the Flux.jl package.

4. Comparison of our Laplace approximation versus the exact calculation

Figure 11 shows the profile likelihoods for a given parameter set (for a random individual). These fix all but the parameter of interest and allow that to vary over some interval. The orange dots show our approximation and we can see strong agreement between the approximation and the “exact” likelihood. The maximum (absolute) error computed over the points shown in the plot is $< 1e - 7$.

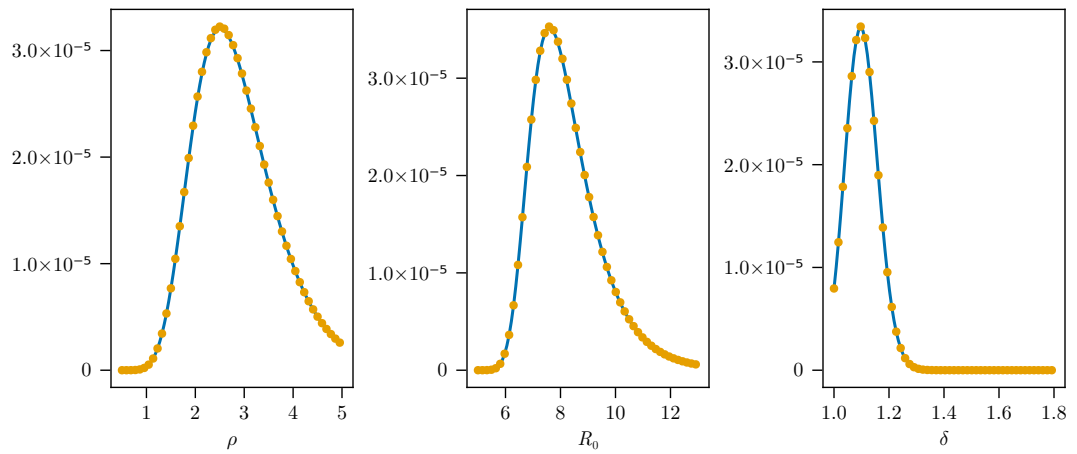


Fig 11. Profile likelihoods for the exact method and the Laplace approximation. Profile likelihoods for the two methods: exact given by the solid blue line, Laplace approximation in orange points.

References

1. Perelson AS. Modelling Viral and Immune System Dynamics. *Nature Reviews Immunology*. 2002;2:28–36. doi:10.1038/nri700.
2. Baccam P, Beauchemin C, Macken CA, Hayden FG, Perelson AS. Kinetics of Influenza A Virus Infection in Humans. *Journal of Virology*. 2006;80:7590–7599. doi:10.1128/JVI.01623-05.
3. Canini L, Perelson AS. Viral Kinetic Modeling: State of the Art. *Journal of pharmacokinetics and pharmacodynamics*. 2014;41:431–443. doi:10.1007/s10928-014-9363-3.
4. Kissler SM, Fauver JR, Mack C, Olesen SW, Tai C, Shiue KY, et al. Viral Dynamics of Acute SARS-CoV-2 Infection and Applications to Diagnostic and Public Health Strategies. *PLOS Biology*. 2021;19:e3001333. doi:10.1371/journal.pbio.3001333.
5. Zitzmann C, Ke R, Ribeiro RM, Perelson AS. How Robust Are Estimates of Key Parameters in Standard Viral Dynamic Models? *PLOS Computational Biology*. 2024;20:e1011437. doi:10.1371/journal.pcbi.1011437.
6. Kissler SM, Fauver JR, Mack C, Tai CG, Breban MI, Watkins AE, et al. Viral Dynamics of SARS-CoV-2 Variants in Vaccinated and Unvaccinated Persons. *New England Journal of Medicine*. 2021;385:2489–2491. doi:10.1056/NEJMc2102507.
7. Serena L, Marzolla M, D'Angelo G, Ferretti S. A Review of Multilevel Modeling and Simulation for Human Mobility and Behavior. *Simulation Modelling Practice and Theory*. 2023;127:102780. doi:10.1016/j.simpat.2023.102780.
8. Ke R, Martinez PP, Smith RL, Gibson LL, Mirza A, Conte M, et al. Daily Longitudinal Sampling of SARS-CoV-2 Infection Reveals Substantial Heterogeneity in Infectiousness. *Nature Microbiology*. 2022;7:640–652. doi:10.1038/s41564-022-01105-z.
9. Néant N, Lingas G, Le Hingrat Q, Ghosn J, Engelmann I, Lepiller Q, et al. Modeling SARS-CoV-2 Viral Kinetics and Association with Mortality in Hospitalized Patients from the French COVID Cohort. *Proceedings of the National Academy of Sciences*. 2021;118:e2017962118. doi:10.1073/pnas.2017962118.
10. Ashcroft P, Lehtinen S, Bonhoeffer S. Test-Trace-Isolate-Quarantine (TTIQ) Intervention Strategies after Symptomatic COVID-19 Case Identification. *PLOS ONE*. 2022;17:e0263597. doi:10.1371/journal.pone.0263597.
11. Challenger JD, Foo CY, Wu Y, Yan AWC, Marjaneh MM, Liew F, et al. Modelling Upper Respiratory Viral Load Dynamics of SARS-CoV-2. *BMC Medicine*. 2022;20:25. doi:10.1186/s12916-021-02220-0.
12. Ke R, Zitzmann C, Ho DD, Ribeiro RM, Perelson AS. In Vivo Kinetics of SARS-CoV-2 Infection and Its Relationship with a Person's Infectiousness. *Proceedings of the National Academy of Sciences*. 2021;118:e2111477118. doi:10.1073/pnas.2111477118.
13. Ciupe SM, Heffernan JM. In-Host Modeling. *Infectious Disease Modelling*. 2017;2:188–202. doi:10.1016/j.idm.2017.04.002.

14. Li K, Cao P, McCaw JM. Modelling the Effect of MUC1 on Influenza Virus Infection Kinetics and Macrophage Dynamics. *Viruses*. 2021;13:850. doi:10.3390/v13050850.
15. Bai F, Allen LJS. Probability of a Major Infection in a Stochastic Within-Host Model with Multiple Stages. *Applied Mathematics Letters*. 2019;87:1–6. doi:10.1016/j.aml.2018.07.022.
16. Barbour AD, Hamza K, Kaspi H, Klebaner FC. Escape from the Boundary in Markov Population Processes. *Advances in Applied Probability*. 2015;47:1190–1211. doi:10.1239/aap/1449859806.
17. Morris D, Maclean J, Black AJ. Computation of Random Time-Shift Distributions for Stochastic Population Models. *Journal of Mathematical Biology*. 2024;89:33. doi:10.1007/s00285-024-02132-6.
18. Germano DPJ, Zarebski AE, Hautphenne S, Moss R, Flegg JA, Flegg MB. A Hybrid Framework for Compartmental Models Enabling Simulation-Based Inference; 2024.
19. Saenz RA, Quinlivan M, Elton D, MacRae S, Blunden AS, Mumford JA, et al. Dynamics of Influenza Virus Infection and Pathology. *Journal of Virology*. 2010;84:3974–3983. doi:10.1128/jvi.02078-09.
20. Hay JA, Kennedy-Shaffer L, Kanjilal S, Lennon NJ, Gabriel SB, Lipsitch M, et al. Estimating Epidemiologic Dynamics from Cross-Sectional Viral Load Distributions. *Science*. 2021;373. doi:10.1126/science.abh0635.
21. Odaka M, Inoue K. Modeling Viral Dynamics in SARS-CoV-2 Infection Based on Differential Equations and Numerical Analysis. *Heliyon*. 2021;7:e08207. doi:10.1016/j.heliyon.2021.e08207.
22. Gillespie DT. Exact Stochastic Simulation of Coupled Chemical Reactions. *The Journal of Physical Chemistry*. 1977;81:2340–2361. doi:10.1021/j100540a008.
23. Gillespie DT. Approximate Accelerated Stochastic Simulation of Chemically Reacting Systems. *The Journal of Chemical Physics*. 2001;115:1716–1733. doi:10.1063/1.1378322.
24. Canini L, Carrat F. Population Modeling of Influenza A/H1N1 Virus Kinetics and Symptom Dynamics. *Journal of Virology*. 2011;85:2764–2770. doi:10.1128/JVI.01318-10.
25. Ciupe SM, Tuncer N. Identifiability of Parameters in Mathematical Models of SARS-CoV-2 Infections in Humans. *Scientific Reports*. 2022;12:14637. doi:10.1038/s41598-022-18683-x.
26. Nguyen VK, Klawonn F, Mikolajczyk R, Hernandez-Vargas EA. Analysis of Practical Identifiability of a Viral Infection Model. *PLOS ONE*. 2016;11:e0167568. doi:10.1371/journal.pone.0167568.
27. Yan AWC, Cao P, McCaw JM. On the Extinction Probability in Models of Within-Host Infection: The Role of Latency and Immunity. *Journal of Mathematical Biology*. 2016;73:787–813. doi:10.1007/s00285-015-0961-5.
28. Ross SM. *Introduction to Probability Models*. Academic Press; 2014.

29. Durrett R. *Essentials of Stochastic Processes*. Springer Texts in Statistics. Cham: Springer International Publishing; 2016.
30. Begon M, Bennett M, Bowers R, French N, Hazel S, Turner J. A Clarification of Transmission Terms in Host-Microparasite Models: Numbers, Densities and Areas. *Epidemiology and Infection*. 2002;129:147–153. doi:10.1017/s0950268802007148.
31. Smith AP, Moquin DJ, Bernhauerova V, Smith AM. Influenza Virus Infection Model With Density Dependence Supports Biphasic Viral Decay. *Frontiers in Microbiology*. 2018;9.
32. Diekmann O, Heesterbeek JAP, Metz JAJ. On the Definition and the Computation of the Basic Reproduction Ratio R_0 in Models for Infectious Diseases in Heterogeneous Populations. *Journal of Mathematical Biology*. 1990;28. doi:10.1007/BF00178324.
33. van den Driessche P, Watmough J. Reproduction Numbers and Sub-Threshold Endemic Equilibria for Compartmental Models of Disease Transmission. *Mathematical Biosciences*. 2002;180:29–48. doi:10.1016/S0025-5564(02)00108-6.
34. Diekmann O, Heesterbeek JaP, Roberts MG. The Construction of Next-Generation Matrices for Compartmental Epidemic Models. *Journal of the Royal Society, Interface*. 2010;7:873–885. doi:10.1098/rsif.2009.0386.
35. Kurtz TG. Solutions of Ordinary Differential Equations as Limits of Pure Jump Markov Processes. *Journal of Applied Probability*. 1970;7:49–58. doi:10.2307/3212147.
36. Curran-Sebastian J, Pellis L, Hall I, House T. Calculation of Epidemic First Passage and Peak Time Probability Distributions; 2023.
37. Marcato AJ, Black AJ, Walker CR, Morris D, Meagher N, Price DJ, et al. Learnings from the Australian First Few X Household Transmission Project for COVID-19. *The Lancet Regional Health - Western Pacific*. 2022;28. doi:10.1016/j.lanwpc.2022.100573.
38. Li K, McCaw JM, Cao P. Enhanced Viral Infectivity and Reduced Interferon Production Are Associated with High Pathogenicity for Influenza Viruses. *PLOS Computational Biology*. 2023;19:e1010886. doi:10.1371/journal.pcbi.1010886.
39. Laurie D. Calculation of Gauss-Kronrod Quadrature Rules. *Mathematics of Computation*. 1997;66:1133–1145. doi:10.1090/S0025-5718-97-00861-2.
40. MacKay DJ. *Information theory, inference and learning algorithms*. Cambridge university press; 2003.
41. Bezanson J, Edelman A, Karpinski S, Shah VB. Julia: A Fresh Approach to Numerical Computing. *SIAM Review*. 2017;59:65–98. doi:10.1137/141000671.
42. Revels J, Lubin M, Papamarkou T. *Forward-Mode Automatic Differentiation in Julia*; 2016.
43. Hernandez-Vargas EA, Velasco-Hernandez JX. In-Host Mathematical Modelling of COVID-19 in Humans. *Annual Reviews in Control*. 2020;50:448–456. doi:10.1016/j.arcontrol.2020.09.006.
44. Beauchemin CA, Handel A. A Review of Mathematical Models of Influenza A Infections within a Host or Cell Culture: Lessons Learned and Challenges Ahead. *BMC Public Health*. 2011;11:S7. doi:10.1186/1471-2458-11-S1-S7.

45. Ejima K, Kim KS, Ludema C, Bento AI, Iwanami S, Fujita Y, et al. Estimation of the Incubation Period of COVID-19 Using Viral Load Data. *Epidemics*. 2021;35:100454. doi:10.1016/j.epidem.2021.100454.
46. Gelman A. *Bayesian Data Analysis*. City: CRC Press; 2013.
47. Sunagawa J, Park H, Kim KS, Komorizono R, Choi S, Ramirez Torres L, et al. Isolation May Select for Earlier and Higher Peak Viral Load but Shorter Duration in SARS-CoV-2 Evolution. *Nature Communications*. 2023;14:7395. doi:10.1038/s41467-023-43043-2.
48. Amos B. Tutorial on Amortized Optimization. *Foundations and Trends® in Machine Learning*. 2023;16:592–732. doi:10.1561/2200000102.
49. Marino J, Cvitkovic M, Yue Y. A General Method for Amortizing Variational Filtering. In: *Advances in Neural Information Processing Systems*. vol. 31. Curran Associates, Inc.; 2018.
50. Gershman S, Goodman N. Amortized Inference in Probabilistic Reasoning. *Proceedings of the Annual Meeting of the Cognitive Science Society*. 2014;36.
51. Rackauckas C, Nie Q. DifferentialEquations.jl – A Performant and Feature-Rich Ecosystem for Solving Differential Equations in Julia. *Journal of Open Research Software*. 2017;5:15. doi:10.5334/jors.151.
52. Innes M, Saba E, Fischer K, Gandhi D, Rudilosso MC, Joy NM, et al. Fashionable Modelling with Flux. *CoRR*. 2018;abs/1811.01457.
53. McCormack CP, Yan AWC, Brown JC, Sukhova K, Peacock TP, Barclay WS, et al. Modelling the Viral Dynamics of the SARS-CoV-2 Delta and Omicron Variants in Different Cell Types. *Journal of the Royal Society, Interface*. 2023;20:20230187. doi:10.1098/rsif.2023.0187.
54. Vehtari A, Gelman A, Simpson D, Carpenter B, Bürkner PC. Rank-Normalization, Folding, and Localization: An Improved \hat{R} for Assessing Convergence of MCMC (with Discussion). *Bayesian Analysis*. 2021;16:667–718. doi:10.1214/20-BA1221.
55. Bédard M. Optimal Acceptance Rates for Metropolis Algorithms: Moving beyond 0.234. *Stochastic Processes and their Applications*. 2008;118:2198–2222. doi:10.1016/j.spa.2007.12.005.
56. Stan Development Team. Stan: A probabilistic programming language; 2024. Available from: <https://mc-stan.org>.
57. Rebuli NP, Bean NG, Ross JV. Hybrid Markov Chain Models of S–I–R Disease Dynamics. *Journal of Mathematical Biology*. 2017;75:521–541. doi:10.1007/s00285-016-1085-2.
58. Kreger J, Komarova NL, Wodarz D. A Hybrid Stochastic-Deterministic Approach to Explore Multiple Infection and Evolution in HIV. *PLOS Computational Biology*. 2021;17. doi:10.1371/journal.pcbi.1009713.
59. Barbour AD. Density Dependent Markov Population Processes. In: Jäger W, Rost H, Tautu P, editors. *Biological Growth and Spread*. Lecture Notes in Biomathematics. Berlin, Heidelberg: Springer; 1980. p. 36–49.

60. Allen LJS. A Primer on Stochastic Epidemic Models: Formulation, Numerical Simulation, and Analysis. *Infectious Disease Modelling*. 2017;2:128–142. doi:10.1016/j.idm.2017.03.001.
61. Black AJ. Importance Sampling for Partially Observed Temporal Epidemic Models. *Statistics and Computing*. 2018;29:617–630. doi:10.1007/s11222-018-9827-1.
62. McKinley TJ, Ross JV, Deardon R, Cook AR. Simulation-Based Bayesian Inference for Epidemic Models. *Computational Statistics & Data Analysis*. 2014;71:434–447. doi:10.1016/j.csda.2012.12.012.
63. Wang X, Wang S, Wang J, Rong L. A Multiscale Model of COVID-19 Dynamics. *Bulletin of Mathematical Biology*. 2022;84:99. doi:10.1007/s11538-022-01058-8.
64. Goyal A, Reeves DB, Schiffer JT. Multi-Scale Modelling Reveals That Early Super-Spreader Events Are a Likely Contributor to Novel Variant Predominance. *Journal of The Royal Society Interface*. 2022;19:20210811. doi:10.1098/rsif.2021.0811.
65. Almocera AES, Nguyen VK, Hernandez-Vargas EA. Multiscale Model Within-Host and between-Host for Viral Infectious Diseases. *Journal of Mathematical Biology*. 2018;77:1035–1057. doi:10.1007/s00285-018-1241-y.
66. Marion G, Hadley L, Isham V, Mollison D, Panovska-Griffiths J, Pellis L, et al. Modelling: Understanding Pandemics and How to Control Them. *Epidemics*. 2022;39:100588. doi:10.1016/j.epidem.2022.100588.
67. Black AJ, Geard N, McCaw JM, McVernon J, Ross JV. Characterising Pandemic Severity and Transmissibility from Data Collected during First Few Hundred Studies. *Epidemics*. 2017;19:61–73. doi:10.1016/j.epidem.2017.01.004.
68. House T, Riley H, Pellis L, Pouwels KB, Bacon S, Eidukas A, et al. Inferring Risks of Coronavirus Transmission from Community Household Data. *Statistical Methods in Medical Research*. 2022;31:1738–1756. doi:10.1177/09622802211055853.
69. Dorman KS, Sinsheimer JS, Lange K. In the Garden of Branching Processes *SIAM Review*. 2004;46:202–229.